Monthly Notices
of the
ROYAL ASTRONOMICAL SOCIETY

Mon. Not. R. Astron. Soc. **406,** 803–821 (2010) doi:10.1111/j.1365-2966.2010.16747.x

The WiggleZ Dark Energy Survey: the selection function and $z = 0.6$ galaxy power spectrum

Chris Blake,[1⋆] Sarah Brough,[1] Matthew Colless,[2] Warrick Couch,[1] Scott Croom,[3] Tamara Davis,[4,5] Michael J. Drinkwater,[4] Karl Forster,[6] Karl Glazebrook,[1] Ben Jelliffe,[3] Russell J. Jurek,[4] I-hui Li,[1] Barry Madore,[7] Chris Martin,[6] Kevin Pimbblet,[8] Gregory B. Poole,[1] Michael Pracy,[1] Rob Sharp,[2] Emily Wisnioski,[1] David Woods[9] and Ted Wyder[6]

[1]*Centre for Astrophysics & Supercomputing, Swinburne University of Technology, PO Box 218, Hawthorn, VIC 3122, Australia*
[2]*Anglo-Australian Observatory, PO Box 296, Epping, NSW 2121, Australia*
[3]*School of Physics, University of Sydney, NSW 2006, Australia*
[4]*Department of Physics, University of Queensland, Brisbane, QLD 4072, Australia*
[5]*Dark Cosmology Centre, Niels Bohr Institute, University of Copenhagen, Juliane Maries Vej 30, DK-2100 Copenhagen, Denmark*
[6]*California Institute of Technology, MC 405-47, 1200 East California Boulevard, Pasadena, CA 91125, USA*
[7]*Observatories of the Carnegie Institute of Washington, 813 Santa Barbara St., Pasadena, CA 91101, USA*
[8]*School of Physics, Monash University, Clayton, VIC 3800, Australia*
[9]*Department of Physics and Astronomy, University of British Columbia, 6224 Agricultural Road, Vancouver, BC V6T 1Z1, Canada*

Accepted 2010 March 26. Received 2010 March 25; in original form 2009 May 11

ABSTRACT

We report one of the most accurate measurements of the three-dimensional large-scale galaxy power spectrum achieved to date, using 56 159 redshifts of bright emission-line galaxies at effective redshift $z \approx 0.6$ from the WiggleZ Dark Energy Survey at the Anglo-Australian Telescope. We describe in detail how we construct the survey selection function allowing for the varying target completeness and redshift completeness. We measure the total power with an accuracy of approximately 5 per cent in wavenumber bands of $\Delta k = 0.01\,h\,\mathrm{Mpc}^{-1}$. A model power spectrum including non-linear corrections, combined with a linear galaxy bias factor and a simple model for redshift-space distortions, provides a good fit to our data for scales $k < 0.4\,h\,\mathrm{Mpc}^{-1}$. The large-scale shape of the power spectrum is consistent with the best-fitting matter and baryon densities determined by observations of the cosmic microwave background radiation. By splitting the power spectrum measurement as a function of tangential and radial wavenumbers, we delineate the characteristic imprint of peculiar velocities. We use these to determine the growth rate of structure as a function of redshift in the range $0.4 < z < 0.8$, including a data point at $z = 0.78$ with an accuracy of 20 per cent. Our growth rate measurements are a close match to the self-consistent prediction of the Λ cold dark matter model. The WiggleZ survey data will allow a wide range of investigations into the cosmological model, cosmic expansion and growth history, topology of cosmic structure and Gaussianity of the initial conditions. Our calculation of the survey selection function will be released at a future date via our website wigglez.swin.edu.au.

Key words: surveys – cosmological parameters – large-scale structure of Universe.

1 INTRODUCTION

The pattern of density fluctuations in the low-redshift Universe results from the physical processes which govern the evolution of matter perturbations after the big bang. In the early Universe, the primordial spectrum of fluctuations created by inflation is processed before recombination in a manner depending on the physical matter density, baryon fraction and massive neutrino fraction (e.g. Bond & Efstathiou 1984; Bardeen et al. 1986; Holtzman 1989; Hu & Sugiyama 1996; Eisenstein & Hu 1998). After recombination, perturbations of all scales are amplified by gravity at an identical rate

⋆E-mail: cblake@astro.swin.edu.au

whilst linear theory applies. This growth rate depends on the matter and dark energy components, which drive the cosmic expansion (e.g. Heath 1977; Hamilton 2001; Linder & Jenkins 2003; Percival 2005). The growth of fluctuations enters a non-linear regime at progressively larger scales at lower redshifts: in today's Universe, only perturbations with Fourier wavescales $k < 0.1\,h\,\mathrm{Mpc}^{-1}$ evolve linearly to a good approximation (e.g. Smith et al. 2003; Jeong & Komatsu 2006; McDonald 2007).

The clustering pattern of galaxies at different redshifts is related to the underlying density fluctuations and may be used to test this model of structure formation. The shape of the clustering power spectrum – the relative amplitudes of large-scale and small-scale modes – depends on the composition of the early Universe and may be used to extract information about the matter and baryon fractions (e.g. Tegmark et al. 2004a; Cole et al. 2005; Percival et al. 2007b). The amplitude of the clustering power spectrum as a function of redshift, together with the pattern of redshift-space distortions induced by galaxy peculiar velocities, can be used to measure the growth rate of structure (e.g. Hamilton 1992; Hawkins et al. 2003; Guzzo et al. 2008; Percival & White 2009). Higher order or topological descriptors of the density field, such as the bispectrum or genus, can be applied to test whether the initial conditions are consistent with scale-invariant Gaussian random perturbations generated by inflation (e.g. Gott, Dickinson & Melott 1986; Fry & Scherrer 1994; James, Lewis & Colless 2007; Sefusatti & Komatsu 2007).

The interpretation of the shape and amplitude of the galaxy power spectrum is complicated by several factors. First, the manner in which galaxies trace the density field – the 'galaxy bias' – is in general a complex function of scale, dark matter halo mass, galaxy type and redshift (Dekel & Lahav 1999; Tegmark & Bromley 1999; Conway et al. 2005; Wild et al. 2005; Smith, Scoccimarro & Sheth 2007; Percival et al. 2007a; Cresswell & Percival 2009). However, the bias of galaxy fluctuations on sufficiently large scales ($k < 0.1\,h\,\mathrm{Mpc}^{-1}$ at $z = 0$) appears to be well described by a simple constant of proportionality whose value depends on galaxy type and luminosity, or more fundamentally dark matter halo mass (Peacock & Dodds 1994; Scherrer & Weinberg 1998; Verde et al. 2002). Secondly, small-scale density perturbations eventually begin to evolve in a non-linear fashion requiring more complex modelling techniques such as higher order perturbation theory or numerical N-body simulations (Smith et al. 2003; Jeong & Komatsu 2006; McDonald 2007). Thirdly, there is a practical challenge of acquiring galaxy survey data across a 'fair sample' of the Universe (Tegmark 1997). For the large-scale linear modes of clustering, which provide the most robust link to underlying theory, this sample must map a volume of the order of 1 Gpc^3 using a sample containing of the order of 10^5 galaxies. These demands require multiyear campaigns with ground-based telescopes utilizing hundreds of clear nights (Glazebrook & Blake 2005).

Despite these challenges, a series of galaxy redshift surveys have been undertaken to provide such data sets at redshifts $z < 0.5$. The state-of-the-art projects which have mapped the 'local' ($z \approx 0.1$) Universe are the 2-degree Field Galaxy Redshift Survey (2dFGRS; Colless et al. 2001) and the Sloan Digital Sky Survey (SDSS; York et al. 2000). The 2dFGRS obtained redshifts for 2×10^5 galaxies covering 1500 deg^2 in the period between 1997 and 2002. The 'main' spectroscopic survey of the SDSS gathered 8×10^5 galaxy redshifts over 8000 deg^2 between 2000 and 2005. The SDSS project also included observations of 1×10^5 luminous red galaxies (LRGs) reaching up to a redshift $z = 0.5$ (Eisenstein et al. 2001).

These data sets have provided a rich source of information about the clustering of galaxies. For example, power spectra have been extracted for the 2dFGRS by Percival et al. (2001) and Cole et al. (2005); for the SDSS 'main' galaxy sample by Pope et al. (2004), Tegmark et al. (2004a) and Percival et al. (2007a); and for the LRGs by Eisenstein et al. (2005), Huetsi (2006), Tegmark et al. (2006) and Percival et al. (2007b). Analysis of these surveys, in combination with the cosmic microwave background fluctuations, has confirmed that we inhabit a low-density Universe where matter today provides only 25–30 per cent of the total energy governing the large-scale dynamics, with the rest located in a mysterious 'dark energy' component. In addition the baryonic fraction of the matter is only 15–20 per cent, with the remainder composed of non-baryonic, cold particles whose nature is currently unknown (e.g. Percival et al. 2002; Tegmark et al. 2004b, 2006; Komatsu et al. 2009). The clustering pattern is also sensitive to the presence of hot dark matter such as massive neutrinos, which comprise a small fraction of the energy budget (Elgaroy et al. 2002; Seljak et al. 2005).

These galaxy surveys also describe how the underlying density fluctuations are modulated by galaxy bias (Verde et al. 2002; Wild et al. 2005; Conway et al. 2005; Percival et al. 2007a; Cresswell & Percival 2009). In this context the comparison of power spectrum measurements from the 2dFGRS and SDSS, which targeted galaxy populations selected in blue and red optical wavebands, respectively, is of particular interest. When the differing galaxy types in these surveys are assigned linear bias factors, the resulting model fits to the linear-regime power spectra produce best-fitting matter densities which are inconsistent at the statistical level of 2σ. Careful treatment of scale-dependent and luminosity-dependent galaxy bias can potentially explain this discrepancy (Percival et al. 2007a; Sanchez & Cole 2008).

There are strong motivations for extending these large-scale structure measurements to higher redshifts ($z > 0.5$). First, the growth of structure implies that the linear regime of evolving perturbations extends to smaller scales at higher redshifts, enabling cleaner and more accurate model fits. Secondly, the shape of the survey cone allows access to significantly greater cosmic volumes at higher redshift, enabling more accurate determinations of the large-scale power spectrum amplitude. Thirdly, baryon oscillations in galaxy power spectra at different redshifts may be used as a standard ruler to extract the cosmic distance–redshift relation and infer the properties of dark energy (Blake & Glazebrook 2003; Hu & Haiman 2003; Seo & Eisenstein 2003). Fourthly, measurements of the growth of cosmic structure as a function of redshift increase our ability to discriminate between dark energy models including modifications to Einstein's theory of gravity (Guzzo et al. 2008; Wang 2008; White, Song & Percival 2009).

Our current tools for probing the matter power spectrum at redshifts $z > 0.5$ are limited. The clustering of high-redshift quasars has been studied by the 2dF Quasar Survey (Outram et al. 2003) and the SDSS (Ross et al. 2009), but the scarcity of quasi-stellar objects implies that the large-scale clustering measurements are strongly limited by shot noise. Photometric redshifts from imaging surveys have been used to study the projected clustering pattern in redshift slices (Blake et al. 2007; Padmanabhan et al. 2007). However, this approach loses the information from small-scale radial clustering modes (Blake & Bridle 2005) and in particular prevents the extraction of the patterns of peculiar velocities, which are swamped by photometric redshift errors. Alternatively, fluctuations in the Lyman α forest absorption spectrum on the sightlines to bright quasars have been used to infer the amplitude of small-scale clustering fluctuations in the high-redshift Universe (Croft et al. 2002; McDonald et al. 2005, 2006). However, this method is

potentially susceptible to systematic modelling errors and is only applicable at redshifts $z > 2.3$ where the Lyman α absorption lines pass into optical wavebands.

The WiggleZ Dark Energy Survey at the Anglo-Australian Telescope (AAT; Drinkwater et al. 2010) will provide the next step forwards in large-scale spectroscopic galaxy redshift surveys, mapping a cosmic volume of the order of 1 Gpc^3 over the redshift range $z < 1$. The survey, which began in 2006 August and is scheduled to finish in 2010 July, is obtaining a sample containing of the order of 200 000 UV-selected emission-line galaxies covering equatorial sky of the order of 1000 deg^2. The principal scientific goal is to measure baryon oscillations in the galaxy power spectrum in redshift bins up to $z = 1$ and provide a robust measurement of the dark energy model. The data set will also trace the density field over unprecedented cosmic volumes at $z > 0.5$, providing a sample comparable to the SDSS LRG catalogue at $z < 0.5$. Moreover, the spatial overlap between the WiggleZ and LRG catalogues in the redshift range $0.3 < z < 0.5$ will allow careful studies of the systematic effects of galaxy bias on power spectrum estimation.

This paper presents a determination of the current WiggleZ survey selection function and galaxy power spectrum, using a data set comprising a fraction of the order of 25 per cent of the final survey observations. The selection function, which describes the angular and radial survey coverage in the absence of clustering, is complicated by the relatively high level of incompleteness in the survey affecting both the parent target catalogues and the spectroscopic follow-up observations (although this latter type of incompleteness will decrease as the survey progresses). However, we demonstrate that despite these complications the galaxy clustering power spectrum may be successfully extracted and already provides accurate tests of the cosmological model that rival lower redshift surveys.

The structure of this paper is as follows. In Section 2, we present a detailed account of the survey selection function including the coverage masks, completeness of our UV imaging catalogues, variations in redshift completeness, redshift distribution as a function of sky position and redshift blunder rate. In Section 3, we describe our power spectrum calculation and its correction for redshift blunders. We compare the predictions of cosmological models to the resulting power spectra in Section 4 and itemize our conclusions in Section 5. We note that we construct our selection function for a fiducial flat Λcold dark matter (ΛCDM) cosmological model with matter density $\Omega_\mathrm{m} = 0.3$.

2 WIGGLEZ SURVEY SELECTION FUNCTION

An overview of the WiggleZ survey observing strategy and galaxy selection criteria is presented by Blake et al. (2009) and Drinkwater et al. (2010) and summarized in Table 1. Briefly, targets are chosen by a joint selection in UV and optical wavebands, using observations by the *Galaxy Evolution Explorer* (*GALEX*) satellite matched with ground-based optical imaging. A series of magnitude and colour cuts is used to preferentially select high-redshift star-forming galaxies with bright emission lines, which are observed using the AAOmega multi-object spectrograph at the AAT.

The survey selection function $W(\boldsymbol{x})$ expresses the expected mean density of galaxies with spectroscopic redshifts at position $\boldsymbol{x}$, given the angular and luminosity survey selection criteria. An accurate determination of the selection function is essential in order to estimate the power spectrum, which describes the amplitude of fluctuations relative to the mean density.

Determination of the WiggleZ survey selection function is complicated by several factors, which are discussed in the following subsections.

(i) The boundaries of each survey region are determined by the overlapping network of UV and optical imaging coverage (see Section 2.1).

(ii) The magnitude cuts used to select galaxies from the input imaging lie close to the faint completeness thresholds of those surveys. For example, the completeness of the *GALEX* UV data at the survey flux threshold varies with the amount of Galactic foreground dust, inducing a variation in target density with angular position (see Section 2.2).

(iii) The spectroscopic redshift completeness of each AAOmega pointing (i.e. the fraction of observed spectra producing successful redshifts) varies considerably with observing conditions such as astronomical seeing and cloud cover, inducing a variation in the density of successful redshifts with angular position (see Section 2.3).

(iv) The programme of *GALEX* imaging has proceeded simultaneously with the spectroscopic follow-up at the AAT. The expansion of the angular mask of the survey with time must be tracked in order to properly model the angular density of redshifts (see Section 2.3).

(v) The spectroscopic redshift completeness of each AAOmega pointing varies systematically across the spectrograph field of view, decreasing towards the edges where acquisition errors are amplified (see Section 2.4).

(vi) Whilst the survey is unfinished, the optical magnitude distribution of observed galaxies varies with position on the sky owing to the target prioritization scheme used for the observations (Drinkwater et al. 2010). This implies that the galaxy redshift distribution also varies with angular position (see Section 2.5).

(vii) A fraction of the assigned galaxy redshifts are 'blunders' resulting from emission-line mis-identifications. The rate of blunders depends on redshift and hence distorts the true radial galaxy distribution (see Section 2.7).

2.1 Coverage masks

This part of the selection function establishes a (0,1) binary angular coverage mask indicating the availability of input targets.

The boundaries of each WiggleZ survey region are defined by the coverage maps of the UV and optical imaging data within that region. The UV data consist of a series of pointings of the *GALEX* satellite. The *GALEX* field of view is a circle of a radius of $0\overset{\circ}{.}6$; we select sources from a slightly smaller radius of $0\overset{\circ}{.}55$ due to concerns about the *GALEX* photometry at the edges of the field (Morrissey et al. 2007). For the survey regions analysed in this paper, the optical coverage map corresponds to the 4th Data Release of the SDSS.

Table 1. Summary of the WiggleZ survey galaxy selection criteria.

UV magnitude cut	$NUV < 22.8$
Optical magnitude cut	$20 < r < 22.5$
UV colour cut	FUV dropout or $FUV - NUV > 1$
Optical–UV colour cut	$-0.5 < NUV - r < 2$
Optical colour cut	If $g < 22.5$ and $i < 21.5$, then $(r - i) < (g - r - 0.1)$ and $(r - i) < 0.4$

The *GALEX* source catalogues contain small regions of bad data corresponding to scattered light from bright stars adjacent to the field of view. We inspect each *GALEX* field by eye for the presence of these artefacts and define rectangular masks to remove these bad data. These masks encompass a negligible fraction (<1 per cent) of the survey area.

2.2 Variation of parent density with dust and exposure time

This part of the selection function modulates the angular coverage map in accordance with incompleteness in the parent imaging catalogues.

The faint UV magnitude threshold for WiggleZ survey selection, $NUV = 22.8$, is comparable to the magnitude completeness limit of the *GALEX* Medium Imaging Survey (MIS) which provides the targets. The incompleteness of the WiggleZ target catalogue is therefore significant and must be modelled in our selection function, because it determines the baseline target density on the sky in the absence of clustering. We calibrated this incompleteness factor as a function of foreground Galactic dust (quantified by the value of E_{B-V}) and *GALEX* exposure time $t_{\rm exp}$.

The variations of E_{B-V} and $t_{\rm exp}$ across the survey regions analysed in this paper are displayed in Fig. 1. The distribution of exposure time is peaked in the range $1400 < t_{\rm exp} < 1800$ s (the canonical MIS exposure time is 1500 s, equivalent to one orbit of the *GALEX* satellite when overheads are included). However, our analysis also includes fields with lower exposure times $500 < t_{\rm exp} < 1400$ s for which we are still gathering data. In addition, some fields have significantly larger values of $t_{\rm exp}$ if they have been observed as part of other *GALEX* projects. The distribution of dust extinction is broad, peaking at $E_{B-V} \approx 0.04$. Although we correct the UV magnitudes for dust extinction (by an amount $A_{NUV} \approx 8E_{B-V} \approx 0.3$; see Drinkwater et al. 2010), the proximity of our observations to the MIS magnitude threshold induces a variation of completeness with E_{B-V}.

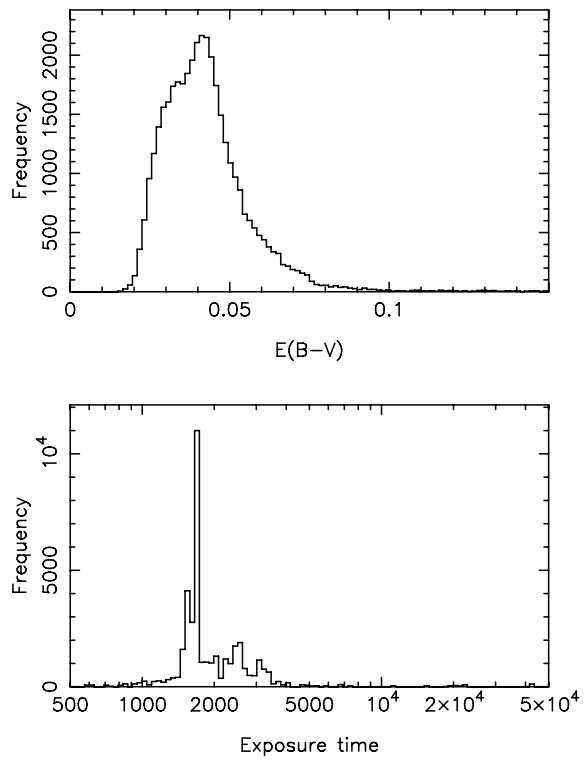

Figure 1. Histograms of the values of *GALEX* exposure time and Galactic dust extinction across the WiggleZ survey regions analysed in this paper.

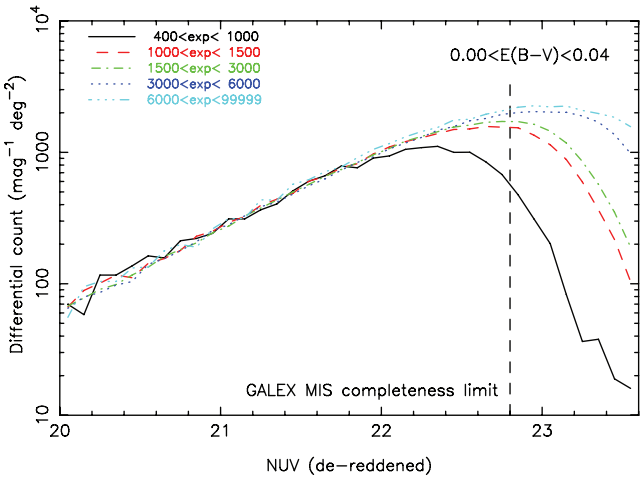

Figure 2. Differential source counts of *GALEX*-SDSS galaxy matches in bins of *GALEX* exposure time. We restrict the analysis to regions of the survey with low dust extinction $E_{B-V} < 0.04$. We note that the uppermost curve with the caption '$6000 < \exp < 99\,999$' corresponds to the 'fiducial' source count in the limit of low dust extinction and high *GALEX* exposure time, as discussed in the text.

We used the *GALEX NUV* (dust-corrected) differential source counts (i.e. counts of galaxies in *NUV* magnitude bins) to calibrate the dependence of the WiggleZ survey completeness on E_{B-V} and $t_{\rm exp}$. For this analysis, we created a *GALEX*-SDSS matched galaxy sample for which we did not impose any of the WiggleZ survey magnitude or colour cuts. This is because the WiggleZ selection cuts reduce the target density by a factor of approximately 6, greatly increasing the noise in these measurements. We matched the *GALEX* NUV catalogues with the SDSS data (using a tolerance of 2.5 arcsec) and removed objects flagged as stars in the SDSS. The presence of these stars would distort the galaxy number counts and induce spurious correlations with E_{B-V} owing to the non-uniform stellar distribution.

We constructed the source count by dividing the survey coverage map into small pixels of a size of $0.^\circ1 \times 0.^\circ1$ and assigning each pixel a mean value of E_{B-V} and $t_{\rm exp}$. We then added up the pixel source counts in bins of E_{B-V} and $t_{\rm exp}$.

Fig. 2 illustrates the source count in bins of exposure time, restricting the analysis to pixels with low dust extinction ($E_{B-V} < 0.04$) in order to isolate the variation with exposure time. We expect to see the number counts rising with increasing magnitude [in the classic Euclidean regime, $\mathrm{d}(\log_{10} N)/\mathrm{d}m = 0.6$] and tailing off at faint magnitudes when incompleteness becomes significant. Indeed, Fig. 2 illustrates that the counts in different exposure time bins agree well at bright magnitudes and the completeness limit grows fainter with increasing exposure time. More detailed fits are presented below.

Fig. 3 displays the counts in bins of E_{B-V} for *GALEX* observations in the exposure time range $1400 < t_{\rm exp} < 1800$ s, in order to isolate the variation with dust extinction. Again, the agreement is good at bright magnitudes (i.e. there is no significant residual dependence of the number counts on dust extinction), and the incompleteness at faint magnitudes increases with the value of E_{B-V}.

We found that a good fitting formula for these source counts as a function of de-reddened magnitude $m = NUV$ is a power law

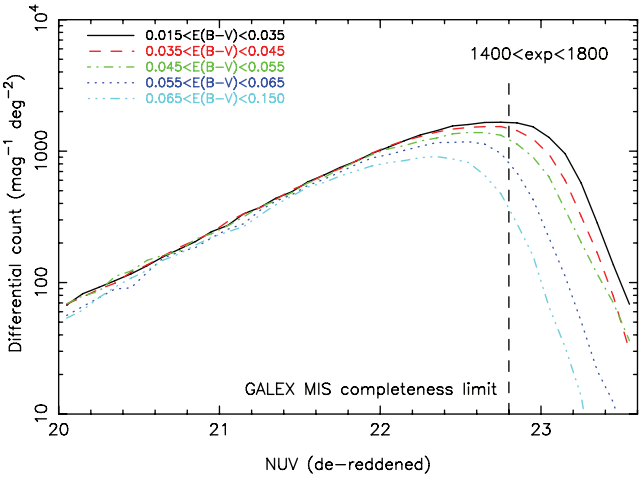

Figure 3. Differential source counts of *GALEX*-SDSS galaxy matches in bins of dust extinction. We restrict the analysis to regions of the survey with *GALEX* exposure times $1400 < t_{\rm exp} < 1800$ s.

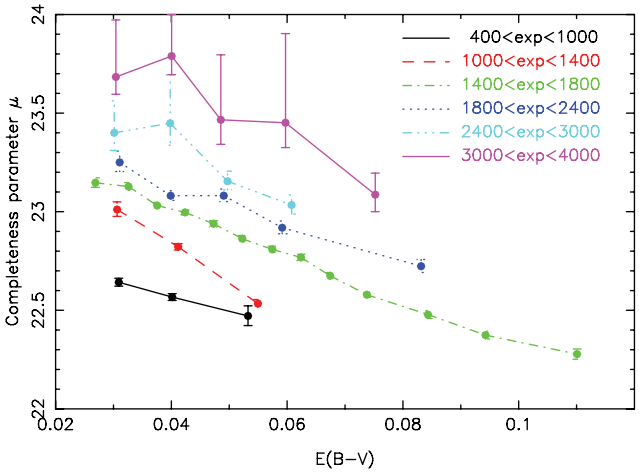

Figure 4. Dependence of the completeness parameter μ on dust extinction, in bins of exposure time. The measurements of μ are of highest quality for the dominant exposure time range $1400 < t_{\rm exp} < 1800$ s. The error range in μ is asymmetric about the best-fitting value because the model becomes increasingly insensitive to μ as the value of μ increases. The measurement for each dust bin is plotted at the median value of E_{B-V} for that bin.

modulated by an incompleteness function:

$$\frac{{\rm d}N}{{\rm d}m}(m) = \frac{{\rm d}N_0}{{\rm d}m}(m) \times C(\mu, \sigma, m), \tag{1}$$

where

$$\frac{{\rm d}N_0}{{\rm d}m}(m) = 10^{\alpha + m\beta} \tag{2}$$

$$C(\mu, \sigma, m) = 0.5 \left[1 + {\rm erf}\left(\frac{\mu - m}{\sigma}\right)\right], \tag{3}$$

where erf(x) is the error function:

$${\rm erf}(x) = \frac{2}{\sqrt{\pi}} \int_0^x \exp(-t^2)\, {\rm d}t. \tag{4}$$

We first fitted equation (1) to the source counts for survey regions in the ranges $E_{B-V} < 0.04$ and $t_{\rm exp} > 6000$ s, which we designated the 'fiducial' source count $C_0(\mu_0, \sigma_0, m)$ in the limit of low dust extinction and high *GALEX* exposure time. The apparent incompleteness in this measurement is not due to *GALEX* observations but to the limiting magnitude threshold of the SDSS data with which we match the *GALEX* sources. We fitted the model to the magnitude range $20.0 < NUV < 22.8$ (motivated by the faint flux threshold for WiggleZ target selection). The best-fitting parameters for the fiducial source count are $\beta = 0.625 \pm 0.013$, $\mu_0 = 22.98 \pm 0.05$ and $\sigma_0 = 1.1 \pm 0.1$, which we assumed for the rest of this analysis. The errors in each parameter are quoted after marginalizing over the remaining parameters. Our derived number counts are consistent with Xu et al. (2005), who show that a model incorporating luminosity evolution provides a good fit to these data. We note that the overall amplitude of the number counts, parametrized by α in equation (2), is not required for determining the incompleteness, as explained below.

We then defined the incompleteness in the *GALEX* catalogues as a function of E_{B-V} and $t_{\rm exp}$, relative to these fiducial counts, by fitting the model:

$$\frac{{\rm d}N}{{\rm d}m}(m) = \frac{{\rm d}N_0}{{\rm d}m}(m) \times C_0(\mu_0, \sigma_0, m) \times C(\mu, \sigma, m). \tag{5}$$

By construction, $C = 1$ in the limit of low dust extinction and high exposure time. We found that the best-fitting value of σ does not vary significantly with dust or exposure time. Therefore, we fixed $\sigma = 0.578$ such that the completeness function depended on just one parameter, μ. We then fitted the value of μ as a function of both E_{B-V} and $t_{\rm exp}$; the results are displayed in Fig. 4, together with the error in μ obtained by marginalizing over the other fitted parameters.

We can compare these results to theoretical expectations. The variation of the completeness limit μ with $t_{\rm exp}$ (at fixed E_{B-V}) agrees well with the theoretical expectation for background-limited imaging of a fixed signal-to-noise ratio, in which a doubling of exposure time equates to approximately 0.4 mag of survey depth. The variation of μ with E_{B-V} (at fixed $t_{\rm exp}$) should follow the dust-extinction law $\Delta\mu \approx 8\ \Delta E_{B-V}$. The observed slope in Fig. 4 is in fact a little steeper, owing to the influence of the additional factor $C_0(m)$ in equation (5).

The completeness of the *GALEX*-SDSS parent catalogue for the UV flux threshold $m_0 = 22.8$ can be determined for a given $\mu(t_{\rm exp}, E_{B-V})$ by evaluating

$${\rm Completeness}(\mu) = \frac{\int_0^{m_0} \frac{{\rm d}N_0}{{\rm d}m}\, C_0(\mu_0, \sigma_0, m)\, C(\mu, \sigma, m)\, {\rm d}m}{\int_0^{m_0} \frac{{\rm d}N_0}{{\rm d}m}\, C_0(\mu_0, \sigma_0, m)\, {\rm d}m}. \tag{6}$$

In order to model the WiggleZ survey target density from these completeness measurements, we must now allow for the fraction of *GALEX*-SDSS matched sources that are selected as WiggleZ targets as a function of *NUV* magnitude. This function is plotted in Fig. 5. WiggleZ targets are preferentially faint in *NUV* owing to the colour selection cut $-0.5 < NUV - r < 2$. We weighted equation (6) with this function in order to determine the WiggleZ survey angular completeness map. We defined this map using a uniform grid of pixels in right ascension and declination.

In Fig. 6, we compare the WiggleZ target densities as a function of dust extinction predicted by our number-counts modelling with the densities observed in the catalogue. We plot the percentage difference of the measured density from the predicted density. The good match indicates that our selection function model is successful. An example parent catalogue completeness map for the 9-h survey region is displayed as Fig. 7(a).

We note that the variation in the angular density of targets is dominated by incompleteness in the UV imaging data rather than in the optical imaging data. Although the faint optical magnitude

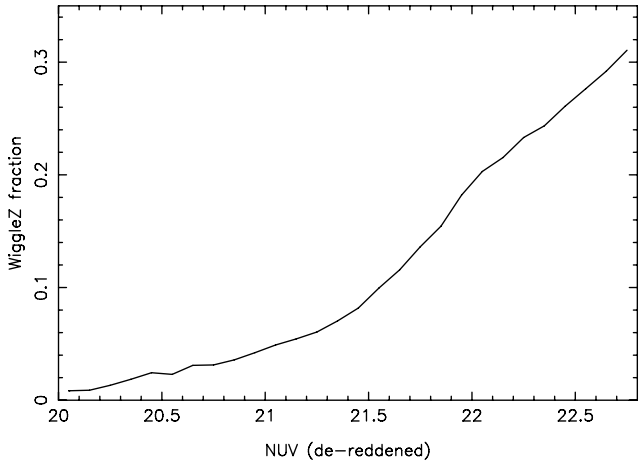

Figure 5. Fraction of *GALEX*-SDSS matches that are selected as WiggleZ targets as a function of *GALEX NUV* magnitude.

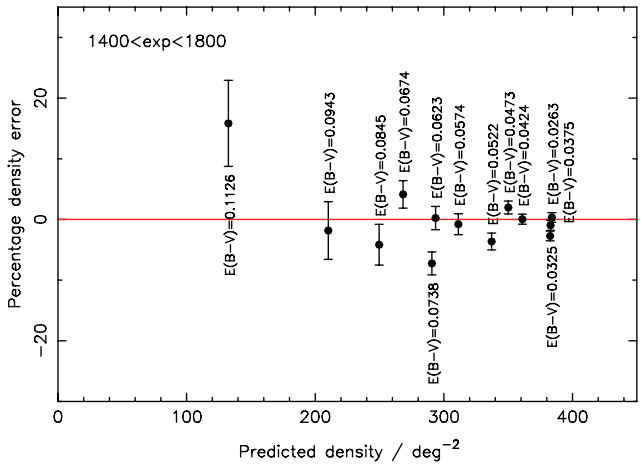

Figure 6. Comparison of the observed and modelled target density for the WiggleZ catalogue in bins of dust extinction for the *GALEX* exposure time range $1400 < t_{\rm exp} < 1800$ s. The average value of E_{B-V} for each dust bin is displayed next to the corresponding data point. Poisson error bars, which are likely to be a mild under-estimate of the true error, are shown for the measured density.

threshold for WiggleZ selection ($r = 22.5$) lies at the completeness limit of the SDSS, the $NUV - r$ colour selection cut implies that the median r-band magnitude of WiggleZ targets is $r \approx 21.5$ and the variation of SDSS completeness with E_{B-V} is negligible. We also studied the variation of completeness with the local astronomical seeing in the SDSS images and found no significant effect on the target densities.

2.3 Redshift completeness map

This part of the selection function samples the density map of the parent target catalogue with the pattern of spectroscopic follow-up observations.

The spectroscopic observations of the WiggleZ survey are defined by a series of AAT pointing centres across each survey region. The pointing centres for each region are determined prior to each survey observing run based upon the available distribution of targets at the time, using a 'simulated annealing' algorithm. Each patch of sky must be observed three to four times on average to build up the WiggleZ redshift catalogue; therefore, we obtain a series of overlapping pointings. Each individual pointing results in a fraction of successful redshifts which varies considerably with astronomical seeing, airmass and cloud cover from under 40 per cent in poor conditions [>2.5 arcsec seeing or airmass sec(z) > 1.5 or over a quarter of the sky covered by cloud] to over 80 per cent in good conditions [<1.5 arcsec seeing and sec(z) < 1.4 and no cloud]. Furthermore, the fraction of successful redshifts in any pointing varies across the field plate of the 2dF spectrograph, as discussed in more detail below. Therefore, as the survey is still partially complete, the redshift completeness map is a complicated function of position on the sky.

We determined the redshift completeness function in each survey region using Monte Carlo realizations of the observations. The steps in the construction of a realization are illustrated in Fig. 7. For each region, we started with the density map as a function of dust and exposure time created by the process described in Section 2.2 (Fig. 7, panel a). We created a Monte Carlo realization of this density map, containing the same number of galaxies as the real target catalogue, by first generating a uniform random catalogue and then excluding points based on a probability equal to the local incompleteness (Fig. 7, panel b). The spectroscopic observations consist of a series of overlapping AAT pointings (Fig. 7, panel c). Each pointing was applied to our realization by laying down a field circle at the correct angular position and randomly assigning the appropriate number of observed sources to spectroscopic fibres.

We note that the available target area has grown over the duration of the survey because the *GALEX* imaging observations are proceeding simultaneously with the redshift follow-up. In the Monte Carlo simulations, it is therefore necessary to track the distribution of *GALEX* tiles available prior to each WiggleZ observing run and only assign target sources to each random realization in areas that were available at the time of each pointing.

For each telescope pointing in the random realization, a fraction of the observed sources are flagged with successful redshifts. The remainder are flagged with unsuccessful redshifts. The total number of successful redshifts for each pointing in the Monte Carlo realization is equal to that achieved in the corresponding survey observation. The probability of a given random source being assigned a successful redshift varies across the field of view of the pointing in the manner described in Section 2.4. The resulting random realization, constructed by applying the full set of pointings, is displayed in Fig. 7, panel (d).

The WiggleZ survey observing strategy involves obtaining repeat spectra of unsuccessful redshifts observed in poor conditions. In addition, a small number of galaxies with existing successful redshifts are re-observed in order to quantify the redshift blunder rate. Each of these categories of observation is included when constructing the Monte Carlo realizations.

2.4 Variation of redshift completeness across the spectrograph field of view

The probability of obtaining a successful redshift in a WiggleZ survey pointing depends on the source position within the spectrograph field of view. We find that galaxies observed at the edges of the field plate have a reduced redshift completeness because these observations are more seriously affected by rotational mis-alignments in target acquisition, which is performed using a limited number of guide-fibre bundles.

Furthermore, we find that the pattern of redshift completeness across the field of view varies between survey observing runs as the spectrograph set-up is re-calibrated, but remains stable

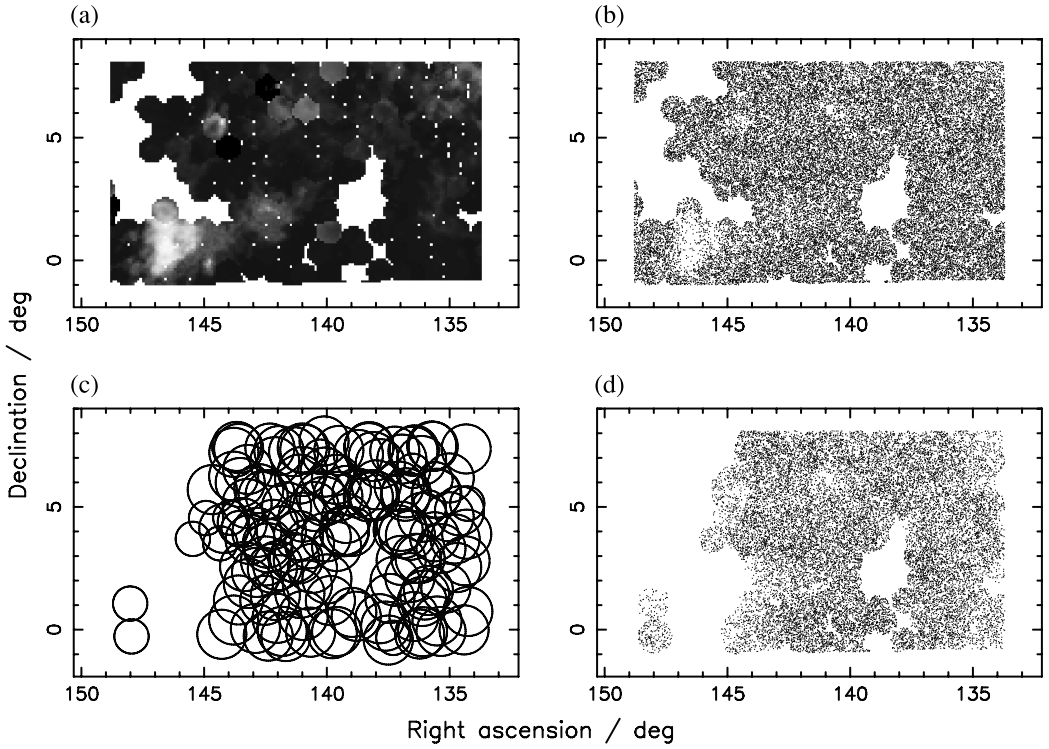

Figure 7. Panels showing for the WiggleZ 9-h region: (a) the angular completeness map of the parent catalogue, (b) a realization of the parent catalogue sampled from this map, (c) the sequence of 2dF field centres and (d) a realization of the redshift catalogue. Note in panel (c) that in some pointings of the survey a field radius of 0.°7 rather than 1.°0 was used, due to concerns over radial-dependent redshift completeness within 2dF pointings.

throughout an observing run. Although individual fibres can be placed in the field of view by the 2dF robot positioner with an accuracy of 20 m (0.3 arcsec), systematic errors can develop in the mapping of (x, y) position on the field plate to (RA, Dec.) position on the sky. These errors are caused by minor discrepancies in the atmospheric correction applied to target apparent positions and (at times during the survey) by an instability in the modelling of optomechanical distortions between the prime focus corrector and the 2dF field plates. These additional errors imply that the redshift completeness variation is not radially symmetric.

These effects are illustrated by Figs 8 and 9. In Fig. 8, we display the radial variation in redshift completeness for WiggleZ survey observing runs between 2007 August and 2008 May. Fig. 9 displays the two-dimensional variation of redshift completeness across the field plate for each of these observing runs, and we use these two-dimensional maps to generate the probabilities of successful redshifts in the Monte Carlo realizations described above. In some observing runs, such as 2007 August, we restricted our spectroscopic observations to the central 0.°7 radius of the 1° radius field of view of the 2dF spectrographs, because the drop in redshift completeness at the edges of the field was particularly significant.

2.5 Radial selection function versus angular position

This part of the selection function creates the appropriate radial distribution of galaxies depending on the distribution of r-band magnitudes in each 2dF pointing.

The final step in the creation of the Monte Carlo realizations is to assign a random redshift to each galaxy, thus establishing the selection function in the radial direction. Targets in the WiggleZ survey are prioritized for observation in accordance with their SDSS r-band magnitudes such that the faintest galaxies are observed earliest in the sequence (Drinkwater et al. 2010). In detail, we use five priority bands which divide the magnitude range $20.0 < r < 22.5$ into equal pieces. Given that there is a correlation between redshift and magnitude, this implies that the survey redshift distribution varies across the sky in a manner dependent on the density of redshifts obtained in a given area.

We track this in our random catalogues by recording for each telescope pointing the number of successful redshifts obtained in each magnitude priority band and assigning these magnitude identifications to sources in the random catalogues. We note that the weak dependence of redshift completeness on the r-band magnitude is also absorbed into this step of the process.

For each magnitude band, we measured the redshift distribution $N(z)$ of successful redshifts using the existing WiggleZ spectroscopic data. In order to reduce the fluctuations due to cosmic variance, we combined the data for the 9-, 11- and 15-h survey regions in this analysis. We used these probability distributions to assign redshifts to random sources on the basis of their magnitude. Fig. 10 plots $N(z)$ for the five magnitude bands for the combined WiggleZ regions. We fit the redshift distributions with a sum of two Gaussian functions and sample the random redshifts from these smooth distributions. Future work will establish $N(z)$ from measurements of the galaxy luminosity function instead.

2.6 Final construction of the survey selection function

The method described in the preceding sub-sections allows us to construct Monte Carlo realizations for each WiggleZ region incorporating the angular and radial variations of the selection function. We can accurately determine the full selection function $W(\boldsymbol{x})$ by stacking together many such realizations: we typically generate 10 000 realizations for each region. We pixelize the selection

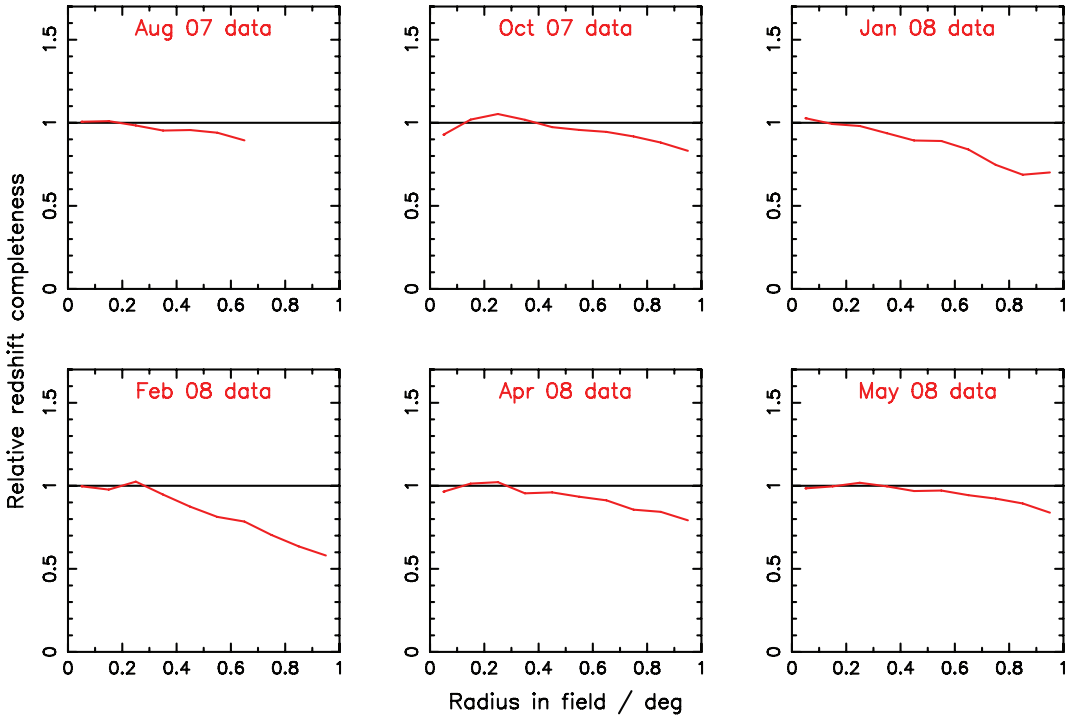

Figure 8. Radial dependence of the redshift completeness in the 2dF for the six WiggleZ survey observing runs between 2007 August and 2008 May. In 2007 August, the field of observation was restricted to radii of $<0.^{\circ}7$. We note that the completeness is normalized relative to a level of 1.0 at the centre of each field.

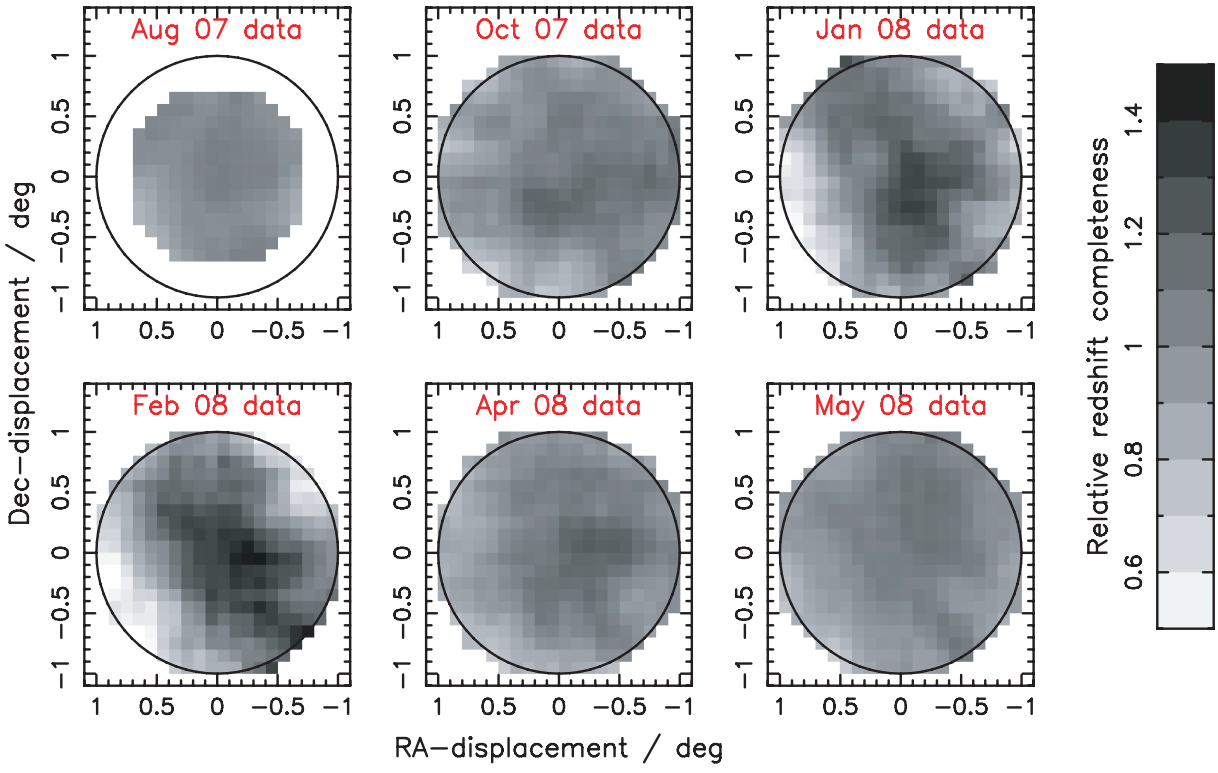

Figure 9. Dependence of the redshift completeness on position in the 2dF for the six WiggleZ survey observing runs between 2007 August and 2008 May. In 2007 August, the field of observation was restricted to radii of $<0.^{\circ}7$. We note that the completeness is normalized relative to a mean level of 1.0 averaged across each field.

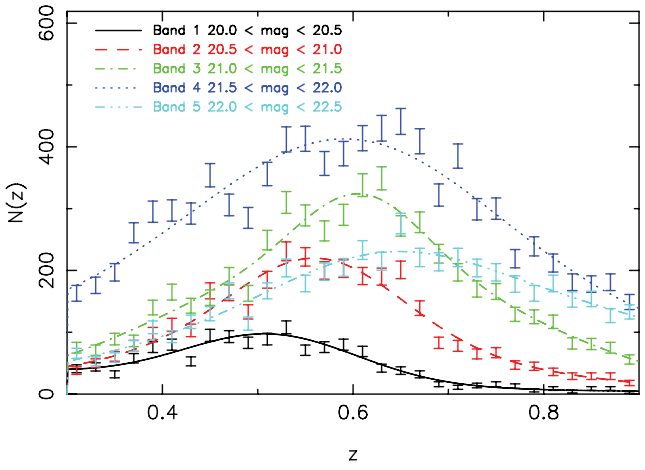

Figure 10. The distribution of WiggleZ redshifts z in the five magnitude bands in which the targets are prioritized. Data are shown for the combined 9-, 11- and 15-h survey regions for the redshift range $0.3 < z < 0.9$ analysed in this paper. Poisson error bars are shown for the points and the data are fitted with a sum of two Gaussian functions.

function in grid cells corresponding to our power spectrum measurement, as discussed in Section 3.1. When converting redshifts to distances, we use a fiducial flat ΛCDM cosmological model with matter density $\Omega_{\rm m} = 0.3$.

2.7 Redshift blunder rate

The redshifts of galaxies in the WiggleZ survey are typically based on identifications of emission lines; the signal-to-noise ratio of the spectra is usually too low to permit detection of the galaxy continuum. The principal line used for redshift identification is the [O II] doublet at a rest-frame wavelength of 3727 Å. This emission line lies in our observed spectral window 4700–9500 Å for the galaxy redshift range $0.26 < z < 1.55$. The redshift identification is confirmed for most galaxies by the additional presence of emission lines such as Hβ 4861 Å, [O III] 4959 Å, [O III] 5007 Å and Hα 6563 Å (Drinkwater et al. 2010).

However, not all redshift identifications are based on multiple emission lines. Features redwards of [O II] progressively leave the observed spectral range with increasing redshift. The Hβ and Hα lines are observable for the ranges $z < 0.95$ and $z < 0.45$, respectively. At relatively high redshifts, the galaxy emission lines must be identified against a background of noisy sky emission lines. Despite these difficulties, we can gain some confidence in single-line redshifts based on [O II] either through detection of the doublet, which is marginally possible with our spectral resolution for galaxies lying at $z > 0.8$, or by eliminating other solutions by failure to detect [O II] at lower wavelengths in cleaner parts of the spectrum.

We assign quality flags from $Q = 1$ (lowest) to $Q = 5$ (highest) for each WiggleZ redshift based on the confidence of our measurement. Redshifts with quality $Q \geq 3$ are considered 'reliable' and used in our analysis. Redshifts with quality $Q \geq 4$ are based on multiple emission lines and are very secure. Galaxies with redshifts based on noisy data or single emission lines are assigned $Q = 3$. The fraction of reliable redshifts with $Q = 3$ is approximately one-third.

Some fraction of WiggleZ redshifts will be blunders. We distinguish two types of redshift blunder for the purposes of our analysis. First, a galaxy emission line may be mis-identified as another, incorrect, emission line. In our power spectrum measurement, this represents (approximately) a convolution of the galaxy density field whereby structures at a given redshift are coherently copied to a second redshift. Secondly, a night-sky emission line may be mis-identified as a galaxy emission line. As there are a large number of night-sky emission lines available for mis-identification, this effectively corresponds to a randomizing of the galaxy density field through the addition of objects whose positions are uncorrelated with the underlying density.

We studied the redshift blunder rate through a programme of repeat observations. In each survey pointing, we assigned a small number of spectrograph fibres (typically three to five) to galaxies which have already been assigned redshifts with quality $Q \geq 3$. We define two redshifts as inconsistent if they differ by $\Delta z > 0.002$ (the typical redshift error for our spectra is $\Delta z = 0.0005$ or 100 km s^{-1}).

We find that pairs of repeat galaxy redshifts which both possess quality $Q \geq 4$ disagree in 2 per cent of cases. Assuming that one of the pairs of inconsistent values is the correct redshift, this implies that the blunder rate for the set of $Q \geq 4$ redshifts is 1 per cent. Pairs of repeat redshifts which both possess $Q = 3$ disagree in 31 ± 2 per cent of cases. However, we can obtain a larger statistical sample for analysis if we consider pairs composed of $Q = 3$ and $Q \geq 4$ redshifts, supposing that the higher quality redshift is the correct value. Under this method we find that the blunder rate of $Q = 3$ redshifts is 17 ± 1 per cent, in good agreement with the internal blunder rate for $Q = 3$ pairs. Given that approximately one-third of reliable redshifts are assigned $Q = 3$, the overall blunder rate for the WiggleZ survey is about 5 per cent. However, we must carefully quantify the redshift blunders in more detail in order to obtain an unbiased measurement of the galaxy power spectrum.

In Fig. 11 we illustrate the fraction of redshift blunders resulting from the mis-identification of an emission line with a second, incorrect, emission line by plotting the distribution of values of $(1 + z_1)/(1 + z_2)$ for inconsistent repeat redshifts composed of $Q = 3$ and $Q \geq 4$ pairs. The values of (z_1, z_2) are the redshifts of the $Q = 3$ and $Q \geq 4$ spectra, respectively. This histogram reveals three significant spikes corresponding to the mis-identification of Hβ, [O III] 5007 Å and Hα as [O II]. Approximately 30 per cent of redshift blunders correspond to this type of mis-identification; the correct redshift in such cases is typically lower than the blunder redshift.

Fig. 12 plots the distribution of redshift blunders not contained in the three spikes in Fig. 11. This type of blunder, comprising about

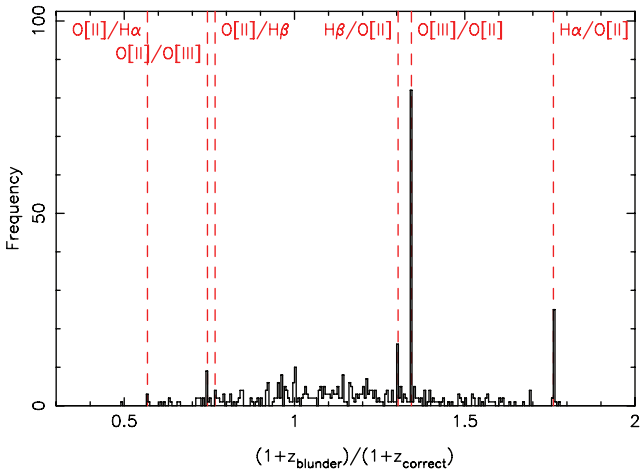

Figure 11. Distribution of values of $(1 + z_1)/(1 + z_2)$ for inconsistent repeat redshifts derived from pairs of spectra with quality flags $Q = 3$ (redshift z_1) and $Q \geq 4$ (redshift z_2). The vertical lines indicate the ratios expected in the cases where Hβ, [O III] and Hα are mis-identified as [O II].

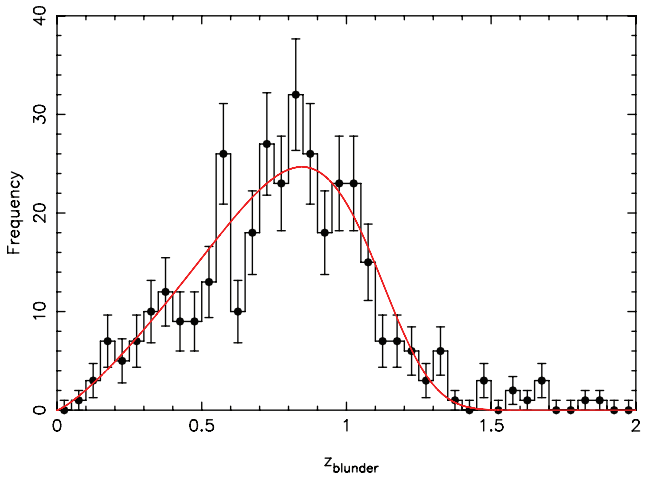

Figure 12. The distribution of redshift blunders for the pairs in Fig. 11 which do not lie in the three prominent spikes. The solid line is the best fit of the model described by equation (7).

70 per cent of all blunders, corresponds to mis-identification of sky emission lines as [O II]. In Fig. 12, we have also fitted a model for the redshift distribution $N(z)$ of the form

$$N(z) \propto \left(\frac{z}{z_0}\right)^{\alpha} \exp\left[-\left(\frac{z}{z_0}\right)^{\beta}\right]. \quad (7)$$

The best-fitting parameters are $z_0 = 1.11, \alpha = 1.24, \beta = 6.46$. We note that the distribution of blunders peaks at a significantly higher redshift than the distribution of correct redshifts shown in Fig. 10. This implies that the blunder fraction varies significantly with redshift – this behaviour is plotted in fig. 6 of Blake et al. (2009). In Section 3.2, we model the effect of these types of redshift blunders on measurements of the galaxy power spectrum.

3 POWER SPECTRUM ANALYSIS

3.1 Power spectrum estimation methodology

In this section we summarize our method of power spectrum estimation, prior to presenting our analysis of the WiggleZ survey data in Section 3.3. Our power spectrum estimation is based on the optimal weighting scheme of Feldman, Kaiser & Peacock (1994, hereafter FKP) (also see the discussions in Tadros & Efstathiou 1996; Hoyle et al. 2002). When converting redshifts to distances, we use a fiducial flat ΛCDM cosmological model with matter density $\Omega_{\rm m} = 0.3$. We first enclosed the survey cone for the particular region and redshift interval within a cuboid of sides (L_x, L_y, L_z) and gridded the galaxy catalogue in cells numbering (n_x, n_y, n_z) using nearest grid point (NGP) assignment to produce a distribution $n(\boldsymbol{x})$. The cell dimensions were chosen such that the Nyquist frequencies in each direction (e.g. $k_{{\rm Nyq},x} = \pi n_x/L_x$) exceeded the maximum frequency of measured power $k_{\rm max}$ by at least a factor of 2 (although we corrected for the effect of NGP assignment on the power spectrum as explained below).

We then applied a fast Fourier transform (FFT) to the grid of data, weighting each pixel by a factor $w(\boldsymbol{x})$ following the method of FKP:

$$\tilde{n}(\boldsymbol{k}) = \sum_{\boldsymbol{x}} n(\boldsymbol{x}) w(\boldsymbol{x}) \exp(\mathrm{i}\boldsymbol{k}\cdot\boldsymbol{x}) \quad (8)$$

where the weighting factor is given by

$$w(\boldsymbol{x}) = \frac{1}{1 + W(\boldsymbol{x}) N_{\rm c} n_0 P_0} \quad (9)$$

(FKP, equation 2.3.4). In equation (9), $N_{\rm c} = n_x n_y n_z$ is the total number of grid cells, $n_0 = N/V$ is the mean number density of galaxies in units of h^3 Mpc^{-3}, where N is the total number of galaxies and $V = L_x L_y L_z$ is the cuboid volume, and P_0 is a characteristic value of the power spectrum at the Fourier wavescale of interest. The purpose of the weighting scheme of equation (9) is given equal weight per volume where we are limited by cosmic variance and equal weight per galaxy where we are limited by shot noise, resulting in an optimal measurement of the power spectrum amplitude $P(k)$ in the case where $P(k) \approx P_0$.

In equation (9), $W(\boldsymbol{x})$ is proportional to the survey selection function determined in Section 2, which describes the number of galaxies expected in each cell $\boldsymbol{x}$ in the absence of clustering. We assume here the normalization

$$\sum_{\boldsymbol{x}} W(\boldsymbol{x}) = 1. \quad (10)$$

We note that summations over cells $\boldsymbol{x}$ may be related to the equivalent integration over volume elements $\mathrm{d}^3\boldsymbol{x}$ by

$$\frac{1}{N_{\rm c}} \sum_{\boldsymbol{x}} W(\boldsymbol{x}) = \frac{1}{V} \int W(\boldsymbol{x})\, \mathrm{d}^3\boldsymbol{x}. \quad (11)$$

We also apply an FFT to the survey selection function:

$$\tilde{W}(\boldsymbol{k}) = \sum_{\boldsymbol{x}} W(\boldsymbol{x}) w(\boldsymbol{x}) \exp(\mathrm{i}\boldsymbol{k}\cdot\boldsymbol{x}). \quad (12)$$

The estimate of the galaxy power spectrum for wavescale $\boldsymbol{k}$ is then

$$P_{\rm est}(\boldsymbol{k}) = \frac{|\tilde{n}(\boldsymbol{k}) - N\tilde{W}(\boldsymbol{k})|^2 - N\sum_{\boldsymbol{x}} W(\boldsymbol{x}) w^2(\boldsymbol{x})}{N^2 N_{\rm c} \sum_{\boldsymbol{x}} W^2(\boldsymbol{x}) w^2(\boldsymbol{x})}. \quad (13)$$

This estimate of the power spectrum is biased by the process of NGP assignment (Jing 2005). In order to remove this bias, we calculated the correction factor for each Fourier mode (by which the power spectrum estimate should be divided):

$$\text{Correction factor}(\boldsymbol{k}) = \frac{\sum_{\boldsymbol{m}} H^2(\boldsymbol{k}') P(\boldsymbol{k}')}{P(\boldsymbol{k})}, \quad (14)$$

where $\boldsymbol{m} = (m_x, m_y, m_z)$ is a vector of integers, $\boldsymbol{k}' = (k'_x, k'_y, k'_z) = (k_x + m_x k_{{\rm Nyq},x}, k_y + m_y k_{{\rm Nyq},y}, k_z + m_z k_{{\rm Nyq},z})$ and

$$H(\boldsymbol{k}) = \frac{\sin\left(\frac{\pi k_x}{2k_{{\rm Nyq},x}}\right) \sin\left(\frac{\pi k_y}{2k_{{\rm Nyq},y}}\right) \sin\left(\frac{\pi k_z}{2k_{{\rm Nyq},z}}\right)}{\left(\frac{\pi k_x}{2k_{{\rm Nyq},x}}\right)\left(\frac{\pi k_y}{2k_{{\rm Nyq},y}}\right)\left(\frac{\pi k_z}{2k_{{\rm Nyq},z}}\right)}. \quad (15)$$

In equation (14), $P(\boldsymbol{k})$ is the underlying model power spectrum. Given that this is initially unknown, we proceed by an iterative approach: we assume a fiducial cosmological model, compute the correction factor, fit cosmological parameters to the power spectrum, re-calculate the correction factor and then repeat the parameter fit. The magnitude of the correction is typically 2 per cent at scale $k \approx 0.2\,h$ Mpc^{-1}.

The spatially varying selection function $W(\boldsymbol{x})$ has two effects on the process of power spectrum estimation. First, the expectation value of equation (13) is the underlying power spectrum $P(\boldsymbol{k})$ convolved with the survey selection function:

$$\langle P_{\rm est}(\boldsymbol{k})\rangle = \frac{\sum_{\boldsymbol{k}'} P(\boldsymbol{k}')|\tilde{W}(\boldsymbol{k} - \boldsymbol{k}')|^2}{N_{\rm c}\sum_{\boldsymbol{x}} W^2(\boldsymbol{x}) w^2(\boldsymbol{x})}. \quad (16)$$

The numerator of equation (16) is summed over the grid points $\boldsymbol{k}'$ in Fourier space for which the FFT of $W(\boldsymbol{x})$ is calculated, i.e.

spaced by $(\Delta k_x, \Delta k_y, \Delta k_z) = (2\pi/L_x, 2\pi/L_y, 2\pi/L_z)$. For reasons of computing speed when fitting models, we re-cast this equation as a matrix multiplication in Fourier bins of width $\Delta k = 0.01\,h\,\mathrm{Mpc}^{-1}$:

$$\langle P_{\rm est}(i)\rangle = \sum_j M_{ij}\, P_{\rm mod}(j). \tag{17}$$

We determine the convolution matrix M_{ij} by evaluating the full sum of equation (16) for a set of unit vectors, e.g. for bin i:

$$P(\boldsymbol{k}) = 1 \quad (k_{i,\rm min} < |\boldsymbol{k}| < k_{i,\rm max}) \tag{18}$$

$$= 0 \quad \text{otherwise.} \tag{19}$$

Secondly, the estimates of the power in different Fourier modes $\boldsymbol{k}$ become correlated. If we average the estimates of equation (13) into bins in Fourier space, labelling the bins by i, the covariance between bins i and j is given by

$$\langle \delta P_i\, \delta P_j\rangle = \frac{2}{N_{\boldsymbol{k}} N_{\boldsymbol{k}'}} \sum_{\boldsymbol{k},\boldsymbol{k}'} |P\,Q(\boldsymbol{k}-\boldsymbol{k}') + S(\boldsymbol{k}-\boldsymbol{k}')|^2 \tag{20}$$

(FKP, equation 2.5.2), where $\boldsymbol{k}$ and $\boldsymbol{k}'$ are pairs of Fourier modes lying in bins i and j, P is the characteristic power spectrum amplitude in bins i and j defined below and the functions $Q(\boldsymbol{k})$ and $S(\boldsymbol{k})$ are given by FKP equations (2.2.3) and (2.2.5), respectively:

$$Q(\boldsymbol{k}) = \frac{\sum_{\boldsymbol{x}} W^2(\boldsymbol{x}) w^2(\boldsymbol{x}) \exp(\mathrm{i}\boldsymbol{k}\cdot\boldsymbol{x})}{\sum_{\boldsymbol{x}} W^2(\boldsymbol{x}) w^2(\boldsymbol{x})} \tag{21}$$

$$S(\boldsymbol{k}) = \left(\frac{1}{n_0 N_{\rm c}}\right) \frac{\sum_{\boldsymbol{x}} W(\boldsymbol{x}) w^2(\boldsymbol{x}) \exp(\mathrm{i}\boldsymbol{k}\cdot\boldsymbol{x})}{\sum_{\boldsymbol{x}} W^2(\boldsymbol{x}) w^2(\boldsymbol{x})}. \tag{22}$$

In deriving equation (20), it is assumed that the power spectrum factor P which appears is effectively constant over Fourier separations $\boldsymbol{k} - \boldsymbol{k}'$ which produce correlated estimates. For our data sets the Fourier transform of the selection function, $\tilde{W}(\boldsymbol{k})$, is sufficiently compact around $k = 0$ that this is a valid approximation. We evaluated equation (20) for each survey region by a direct summation over Fourier modes in the FFT grid. Equation (20) depends on the underlying power spectrum, which is initially unknown, in the same manner as equation (14). We again used an iterative approach whereby we initially used a default model power spectrum to make this calculation and then replaced it using the fitted parameters.

In order to facilitate comparison with other studies, it is useful to take the limit of these equations in the case where the selection function is constant, i.e. $W(\boldsymbol{x}) = 1/N_{\rm c}$. The power spectrum estimator of equation (13) becomes

$$P_{\rm est}(\boldsymbol{k}) = \frac{|\tilde{n}(\boldsymbol{k}) - N\tilde{W}(\boldsymbol{k})|^2 - N}{N^2} \tag{23}$$

and the covariance matrix in equation (20) reduces to a diagonal matrix with entries:

$$\left\langle (\delta P_i)^2 \right\rangle = \frac{2}{N_{\boldsymbol{k}}} \left(P + \frac{1}{n_0}\right)^2, \tag{24}$$

where $N_{\boldsymbol{k}}$ is the number of Fourier modes lying in bin i. Equation (24) clarifies that there are two sources of error in an estimate of the power spectrum: cosmic variance and shot noise, represented by the two terms inside the bracket.

3.2 Redshift blunder correction

In this section, we calculate the distortion in the galaxy power spectrum created by the types of redshift blunder described in Section 2.7. In order to gain intuition, we begin with a simple model using the 'flat-sky approximation' which supposes that galaxies are scattered in position along a single axis of the cuboid (which we take as the x-axis). Defining $\delta(\boldsymbol{x})$ as the galaxy overdensity in the cell at position $\boldsymbol{x} = (x, y, z)$, the galaxy number distribution is given by

$$n(\boldsymbol{x}) = N W(\boldsymbol{x})[1 + \delta(\boldsymbol{x})], \tag{25}$$

where $W(\boldsymbol{x})$ is the selection function normalized as above. We now suppose that a fraction f of galaxies are scattered in position along the x-axis such that their final x-position is drawn from a probability distribution $V(x)$ (i.e. as described by equation 7 for our data). This process creates a scattered galaxy number distribution given by

$$S(\boldsymbol{x}) = N_1 V(x) \sum_{x'} n(x', y, z), \tag{26}$$

where the normalization constant N_1 can be calculated by requiring that $\sum_{\boldsymbol{x}} S(\boldsymbol{x}) = fN$. Equations (25) and (26) have Fourier transforms

$$\tilde{n}(\boldsymbol{k}) = N[\tilde{W}(\boldsymbol{k}) + \tilde{C}(\boldsymbol{k})] \tag{27}$$

$$\tilde{S}(\boldsymbol{k}) = fN\tilde{V}(k_x)[\tilde{W}(0, k_y, k_z) + \tilde{C}(0, k_y, k_z)], \tag{28}$$

where we have defined the convolved density field

$$\tilde{C}(\boldsymbol{k}) = \sum_{\boldsymbol{k}'} \tilde{W}(\boldsymbol{k}' - \boldsymbol{k})\,\tilde{\delta}(\boldsymbol{k}'). \tag{29}$$

It is convenient to subtract the selection function contribution:

$$\tilde{n}'(\boldsymbol{k}) = \tilde{n}(\boldsymbol{k}) - N\tilde{W}(\boldsymbol{k}) \tag{30}$$

$$\tilde{S}'(\boldsymbol{k}) = \tilde{S}(\boldsymbol{k}) - fN\tilde{W}(0, k_y, k_z)\tilde{V}(k_x). \tag{31}$$

We now construct the combined density field $m(\boldsymbol{x}) = (1-f)\,n(\boldsymbol{x}) + S(\boldsymbol{x})$ and write (for the purposes of this calculation) a simple power spectrum estimator

$$P_{\rm est}(\boldsymbol{k}) = \frac{|\tilde{m}'(\boldsymbol{k})|^2 - N}{N^2}, \tag{32}$$

where $\tilde{m}'(\boldsymbol{k}) = (1-f)\tilde{n}'(\boldsymbol{k}) + \tilde{S}'(\boldsymbol{k})$. The terms needed to determine $|\tilde{m}'(k)|^2$ are

$$|\tilde{n}'(\boldsymbol{k})|^2 = (1-f)^2 N^2 |\tilde{C}(\boldsymbol{k})|^2 \tag{33}$$

$$\tilde{n}'^*(\boldsymbol{k})\tilde{S}'(\boldsymbol{k}) = f(1-f)N^2\tilde{V}(k_x)P'(\boldsymbol{k}) \tag{34}$$

$$|\tilde{S}'(\boldsymbol{k})|^2 = f^2 N^2 |\tilde{C}(0, k_y, k_z)|^2 |\tilde{V}(k_x)|^2, \tag{35}$$

where

$$P'(\boldsymbol{k}) = \sum_{\boldsymbol{k}'} P(\boldsymbol{k}')\tilde{W}_{\boldsymbol{k}'-\boldsymbol{k}}\tilde{W}^*_{\boldsymbol{k}'-(0,k_y,k_z).} \tag{36}$$

Writing the convolved power spectrum as $P_{\rm c}(\boldsymbol{k}) = |\tilde{C}(\boldsymbol{k})|^2$, the final result for the power spectrum estimate is

$$P_{\rm est}(\boldsymbol{k}) = (1-f)^2 P_{\rm c}(\boldsymbol{k}) + 2f(1-f)\mathrm{Re}[\tilde{V}(k_x)P'(\boldsymbol{k})] + f^2 P_{\rm c}(0, k_y, k_z)|\tilde{V}(k_x)|^2. \tag{37}$$

In the special case that the selection function and scattering functions are constant, we find that

$$P_{\rm est}(\boldsymbol{k}) = P(\boldsymbol{k}) \qquad (k_x = 0) \tag{38}$$

$$= (1-f)^2 P(\boldsymbol{k}) \qquad (k_x \neq 0). \tag{39}$$

If the Fourier modes $\boldsymbol{k}$ are binned in spherical shells as a function of $k = |\boldsymbol{k}|$ then, as the value of k increases, the contribution of the

mode with $k_x = 0$ becomes less important and $P_{\rm est}(k) = (1-f)^2 P(k)$ is an increasingly good approximation.

We now consider the case where a fraction f of redshifts are scattered by a fixed displacement along the x-axis, i.e. a convolution of the density field by a function U. Equation (26) is replaced by the relation

$$S(\boldsymbol{x}) = N_1 \sum_{x'} n(x', y, z) U(x - x') \tag{40}$$

with the Fourier transform

$$\tilde{S}(\boldsymbol{k}) = f N \tilde{U}(k_x)[\tilde{W}(\boldsymbol{k}) + \tilde{C}(\boldsymbol{k})]. \tag{41}$$

Defining $\tilde{S}'(\boldsymbol{k}) = \tilde{S}(\boldsymbol{k}) - f N \tilde{U}(k_x)\tilde{W}(\boldsymbol{k})$, we find that

$$P_{\rm est}(\boldsymbol{k})/P_{\rm c}(\boldsymbol{k}) = (1-f)^2 + 2f(1-f){\rm Re}[\tilde{U}(k_x)] + f^2|\tilde{U}(k_x)|^2. \tag{42}$$

For a simple shift $U(x) = \delta(x - x_0)$, we find that

$$P_{\rm est}(\boldsymbol{k}) = [1 - 2f(1-f)[1 - \cos(k_x x_0)]\, P(\boldsymbol{k}). \tag{43}$$

These formulae are only approximations in the case of real data. First, the sky is curved and the redshift scatters do not happen along a single axis of the cube. Secondly, the blunder fraction depends on redshift. Thirdly, the blunders due to line confusion are not a strict convolution of the density field, but a transformation in redshift $z_1 \rightarrow z_2$ of the form $z_2 = C(1 + z_1) - 1$, where C is a constant depending on the rest wavelengths of the lines. Fourthly, if a convolved redshift is shifted beyond the edge of the density cube, it does not 'wrap around' as required by periodic boundary conditions. Fifthly, FKP estimation of the power spectrum is used rather than equation (32).

In order to measure the distortion of our measured power spectrum due to redshift blunders for the real data, we therefore created Monte Carlo simulations of galaxy catalogues with a known input power spectrum and the same selection function $W(\boldsymbol{x})$ as each of our survey regions. We then applied the redshift blunder distributions of Figs 11 and 12 to the mock catalogues and re-measured the power spectrum. Comparison of the input and output power spectra, averaging over many Monte Carlo realizations, provided the correction factor due to redshift blunders. We tested our code by reproducing the relations given in equations (37) and (42) in the flat-sky case.

Fig. 13 plots the correction factors for the 'angle-averaged' power spectrum $P(k)$ for each of the survey regions (taking a redshift interval $0.3 < z < 0.9$). We see that a good approximation for the correction for scales $k > 0.05\,h\,{\rm Mpc}^{-1}$ is a constant, although a more significant correction is required for large scales $k < 0.05\,h\,{\rm Mpc}^{-1}$. For $k > 0.05\,h\,{\rm Mpc}^{-1}$ the approximately constant correction factor is not exactly equal to $(1-f)^{-2}$ as predicted by equation (39), where f is the average redshift blunder rate of the catalogue; this is due to the mis-estimation of the denominator of equation (13) that occurs because $W(\boldsymbol{x})$ is determined from the galaxy redshift distribution including blunders, as described in Section 2.5. The Monte Carlo simulations performed here also correct for this small bias in power spectrum estimation.

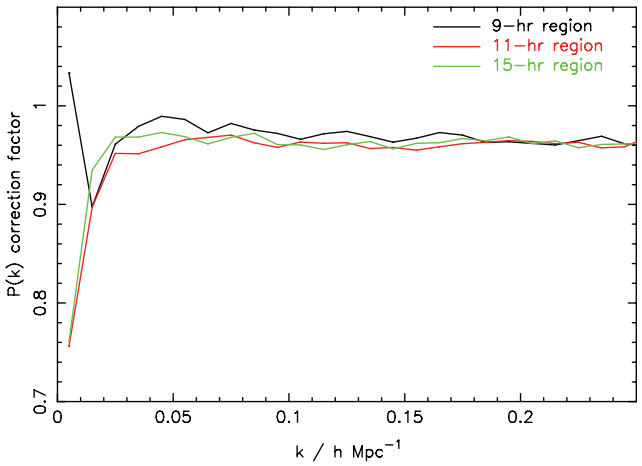

Figure 13. The power spectrum correction factor due to redshift blunders for each of the survey regions analysed in this paper, for a redshift range $0.3 < z < 0.9$. The measured power spectrum must be divided by this factor in order to obtain an unbiased estimate of the true power spectrum.

3.3 Power spectrum measurement

In this study, we analysed a galaxy sample drawn from WiggleZ survey observations prior to 2009 July in SDSS regions of our optical imaging (9, 11 and 15 h). Fig. 14 plots the (RA, Dec.) distribution of these redshifts. We imposed the redshift cut $0.3 < z < 0.9$ in order to remove the tails of the redshift distribution which contain relatively few galaxies. A total of $N = 56\,159$ galaxy redshifts remained. We then split the sample into three redshift slices: $0.3 < z < 0.5$, $0.5 < z < 0.7$ and $0.7 < z < 0.9$.

We determined the effective redshift $z_{\rm eff}$ of our power spectrum estimate in each redshift slice by weighting each pixel in our three-dimensional selection function by its contribution to the power spectrum error:

$$z_{\rm eff}(k) = \sum_{\boldsymbol{x}} z \times \left(\frac{n_{\rm g}(\boldsymbol{x}) P(k)}{1 + n_{\rm g}(\boldsymbol{x}) P(k)} \right)^2, \tag{44}$$

where $n_{\rm g}(\boldsymbol{x}) = (N_{\rm c} N/V) W(\boldsymbol{x})$ is the galaxy number density in each grid cell and $P(k)$ is the power spectrum amplitude. In each case, we used the best-fitting model power spectrum determined below. We evaluated this function at $k = 0.15\,h$ Mpc^{-1}, although the dependence on scale is weak. The effective redshifts of each slice determined using equation (44) are $z_{\rm eff} = (0.42, 0.59, 0.78)$.

We analysed the three WiggleZ survey regions independently, resulting in a total of nine power spectrum measurements. We estimated the power spectrum up to a maximum Fourier wavescale $k_{\rm max} = 0.4\,h$ Mpc^{-1}, assuming the value $P_0 = 2500\,h^{-3}$ Mpc^3 for the weighting factor in equation (9). This choice is motivated by our final measurement of the power spectrum amplitude presented below on scales $k \approx 0.15\,h$ Mpc^{-1}, but does not have a strong influence on our results given that with the survey partially complete the measurements are limited by shot noise on most scales. Representative values for the other parameters in Section 3.1 are $(L_x, L_y, L_z) = (600, 600, 300)\,h^{-1}$ Mpc, $(n_x, n_y, n_z) = (256, 256, 128)$, $V = 0.1\,h^{-3}$ Gpc^3 and $n_0 = 5 \times 10^{-5}\,h^3$ Mpc^{-3}. We combined the Fourier amplitudes in angle-averaged bins of width $\Delta k = 0.01\,h$ Mpc^{-1}.

The nine power spectrum measurements are plotted in Fig. 15 together with a power spectrum model derived using a 'standard' set of cosmological parameters together with a prescription for redshift-space distortions. The details of this model are described in Section 4.1. The dashed and solid lines illustrate the input model, and the model convolved with the selection function for each region, respectively. The model provides an acceptable statistical fit to the measured power spectrum in each case.

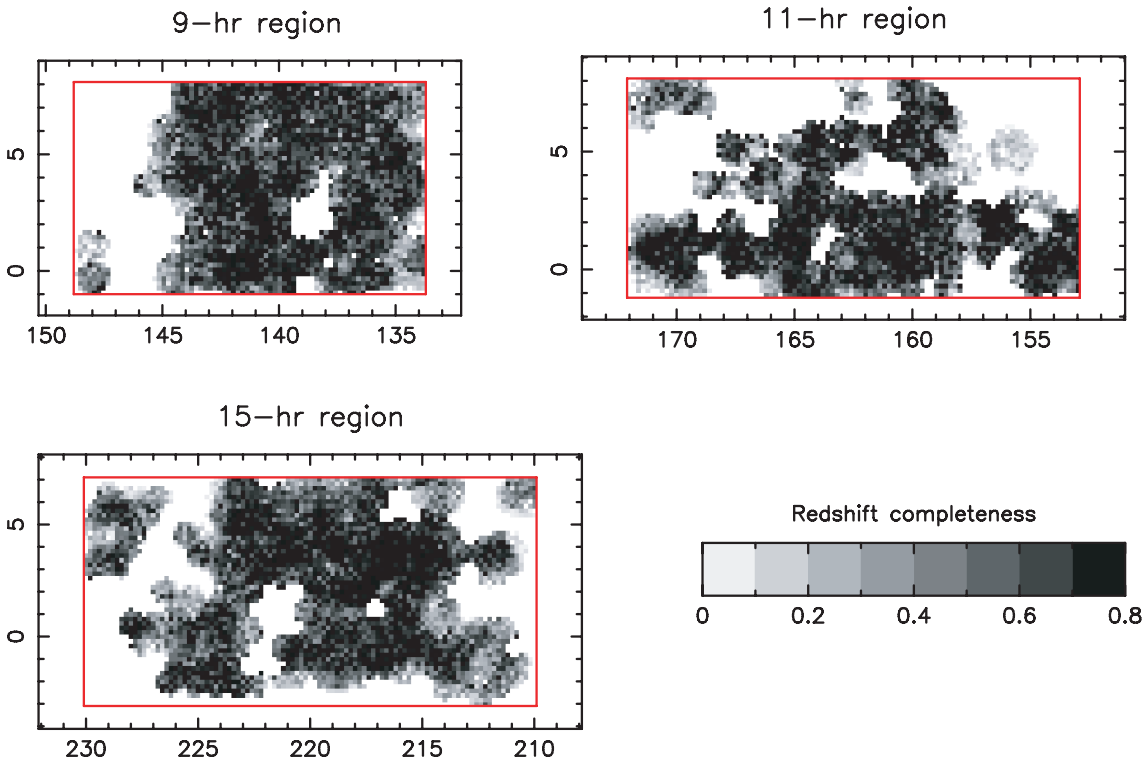

Figure 14. Grey-scale map illustrating the completeness of the spectroscopic follow-up of the WiggleZ targets for the three survey regions analysed in this paper. This figure is generated by taking the ratio of the galaxy densities in the redshift and parent catalogues in small cells. The x-axis and y-axis of each panel are right ascension and declination, respectively.

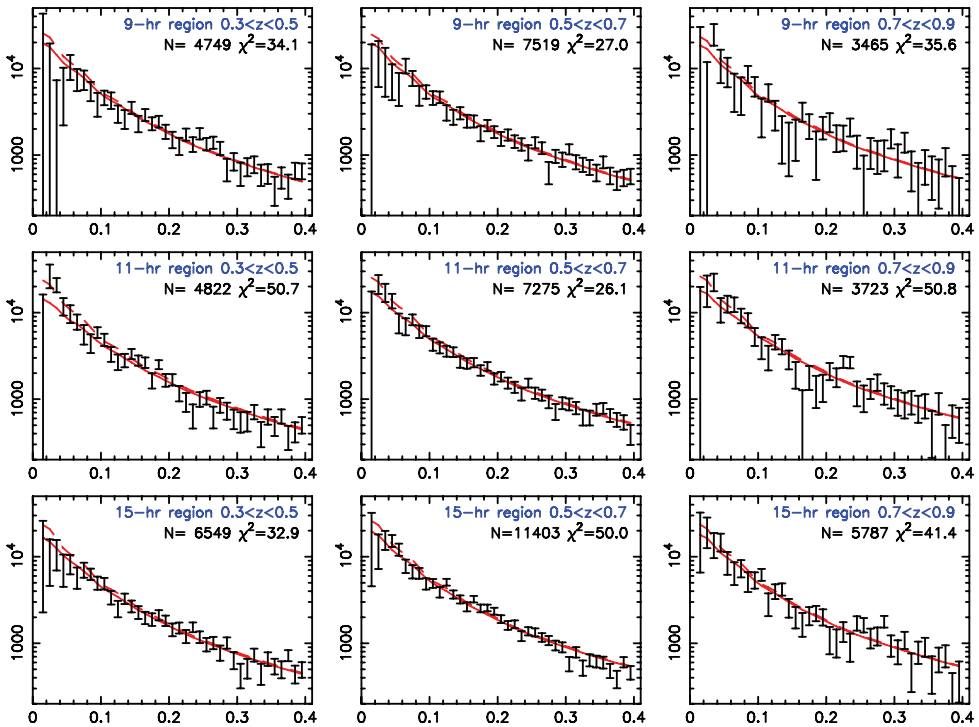

Figure 15. The one-dimensional galaxy power spectrum for each of the survey regions and redshift slices analysed in this paper. The data points in each plot are the power spectrum measured by FKP estimation. The dashed line is an (unconvolved) model power spectrum evaluated by integrating equation (46) over angles. We use cosmological parameters $\Omega_{\rm m} = 0.3$, $\Omega_{\rm b}/\Omega_{\rm m} = 0.166$, $h = 0.72$, $n_{\rm s} = 0.96$ and $\sigma_8 = 0.8$, together with values of the redshift-space distortion parameters and linear bias factor fit to the two-dimensional power spectrum for each redshift slice. The solid line is the result of convolving this model power spectrum with the selection function for each region. The χ^2 statistic is calculated over the range $k < 0.4\,h$ Mpc^{-1} using the full covariance matrix. The x-axis and y-axis of each panel are Fourier wavescale k in units of h Mpc^{-1} and power spectrum amplitude $P(k)$ in units of h^{-3} Mpc^3, respectively.

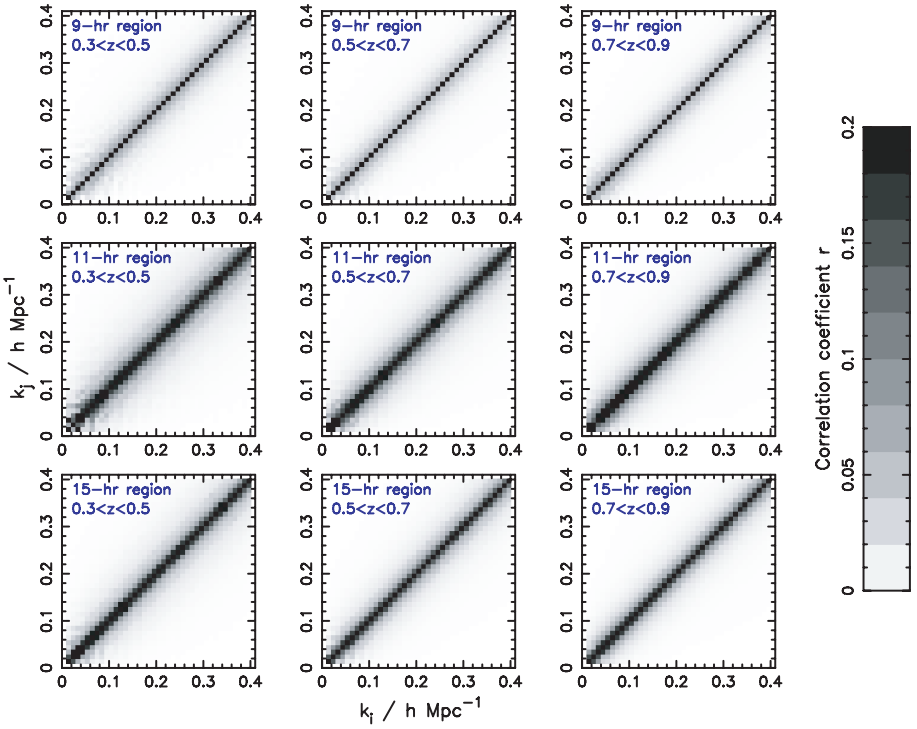

Figure 16. Grey-scale plot of the correlation coefficient r of equation (45) for each of the survey regions and redshift slices analysed in this paper, indicating the degree of covariance between the power spectrum measurement in different Fourier bins. Note the choice of grey-scale range such that the darkest shade corresponds to $r = 0.2$.

The corresponding nine covariance matrices C_{ij} are plotted in Fig. 16 as a correlation coefficient

$$r(i,j) = \frac{C_{ij}}{\sqrt{C_{ii}\,C_{jj}}}. \quad (45)$$

Fig. 16 demonstrates that the amplitude of the off-diagonal elements of the covariance matrices is small (note the choice of grey-scale range).

We also measured power spectra in wavevector bins ($k_{\rm perp}$, $k_{\rm par}$) perpendicular and parallel to the line of sight, respectively (we now use Fourier bins of width $\Delta k = 0.02\,h$ Mpc^{-1} in each direction to increase the signal-to-noise ratio in each bin). This two-dimensional power spectrum allows us to recover the redshift-space distortion parameters which produce an anisotropic galaxy power spectrum. Since in our analysis we orient the x-axis parallel to the line of sight to the centre of each survey region, we make the flat-sky approximation $k_{\rm perp} = \sqrt{k_y^2 + k_z^2}$, $k_{\rm par} = |k_x|$ in this analysis.

3.4 Systematic error study

We investigated the dependence of our power spectrum measurement on potential systematic errors in the survey selection function. In order to do this we re-constructed four different selection functions for the 9-h region, analysing the full redshift range $0.3 < z < 0.9$, with (extreme) variations in the method.

(i) We removed the variation of the completeness of the parent *GALEX*-SDSS sample with dust and *GALEX* exposure time described in Section 2.2 and instead assumed a constant density map.

(ii) We removed the variation of redshift completeness across the field of view of the 2dF spectrograph described in Section 2.4 and instead assumed a constant redshift completeness.

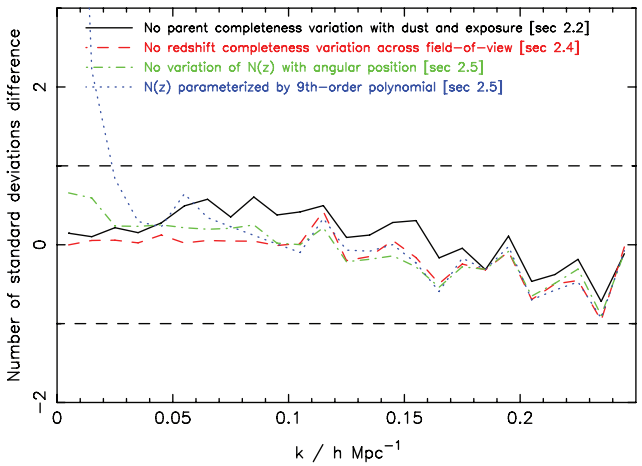

Figure 17. Variations in the power spectrum estimate for the 9-h region, in units of standard deviations in the fiducial power spectrum, obtained by changes in the methodology used to construct the selection function.

(iii) We removed the dependence of the survey redshift distribution on angular position described in Section 2.5 and instead used a position-independent radial selection function.

(iv) We parametrized the redshift distribution for each magnitude slice using a ninth-order polynomial rather than a sum of two Gaussian functions.

In Fig. 17 we plot the difference between the resulting power spectra measured for these four different selection functions and the fiducial power spectrum, in units of the standard deviation of the measurement at each scale. We note that these (extreme) variations in our understanding of the selection function typically cause up

to $\approx 0.5\sigma$ shifts in the power spectrum estimate. The exception is the parametrization of the redshift distribution, which causes large deviations in the very large-scale ($k < 0.03\,h$ Mpc^{-1}) power spectrum. For the example being studied, we noted that the ninth-order polynomial fit was in fact providing a poorer match than the double Gaussian function to the observed redshift distributions, causing a spurious increase in measured large-scale power.

We conclude that our power spectrum measurements are likely to be robust against reasonable systematic variations in the selection function methodology. The selection function in Fourier space is compact and the corrections are only significant on the largest scales.

4 COSMOLOGICAL PARAMETER FITS

In this section, we present some initial comparisons between our power spectrum measurements and cosmological models. Our aim is to establish whether or not our measurements are consistent with the predictions of the standard ΛCDM framework with parameters determined by observations of the cosmic microwave background radiation. Future papers will perform a more comprehensive analysis.

4.1 Model power spectra

We derived model matter power spectra $P_{\rm m}(k)$ as a function of redshift using the CAMB software package (Lewis, Challinor & Lasenby 2000) which is based on CMBFAST (Seljak & Zaldarriaga 1996), including corrections for non-linear growth of structure using the fitting formulae of Smith et al. (2003) (HALOFIT = 1 in CAMB). Throughout this analysis (unless otherwise noted) we fix values for the Hubble parameter $h = 0.72$, scalar index of spectral fluctuations $n_{\rm s} = 0.96$ and normalization $\sigma_8 = 0.8$ and vary only the matter density $\Omega_{\rm m}$ and the baryon fraction $\Omega_{\rm b}/\Omega_{\rm m}$. Our choices of parameter values are consistent with recent observations of the cosmic microwave background radiation (Komatsu et al. 2009).

For this initial parameter fitting, we assumed a linear bias factor b for the galaxy population. The assumption of linear bias will be investigated in more detail in future studies through the use of mock catalogues generated from dark matter simulations, analysis of the galaxy bispectrum (e.g. Verde et al. 2002; Nishimichi et al. 2007) and measurements of the halo occupation distribution of WiggleZ galaxies (e.g. Zehavi et al. 2005; Blake, Collister & Lahav 2008). We note that in the current analysis, the value of the bias factor is significantly degenerate with the choice of σ_8 (such that $b \propto 1/\sigma_8$).

We modified this real-space matter power spectrum to include redshift-space distortions, which we characterized in the standard manner using two parameters. The first parameter, f, models the effect of large-scale coherent infall velocities. In linear theory for the growth of fluctuations, f is related to the linear growth factor $D(a)$ at scalefactor a by $f = {\rm d}\ln D/{\rm d}\ln a$. This functional form is well approximated by $f = \Omega_{\rm m}(z)^{\gamma}$, where $\Omega_{\rm m}(z)$ is the matter density measured by an observer at redshift z, and $\gamma \approx 0.55$ for a standard ΛCDM cosmology. Coherent velocities can also be parametrized by $\beta = f/b$, introducing a dependence on galaxy type via the bias factor. The second parameter, σ_v (in units of h km s^{-1}), describes small-scale random virialized velocities, for which we assumed an exponential pairwise distribution. The overall effect on the galaxy power spectrum $P_{\rm gal}$ is to induce an anisotropic distortion dependent on the angle θ of the wavevector to the line of sight, parametrized by $\mu = \cos\theta$:

$$P_{\rm gal}(k,\mu) = b^2\,P_{\rm m}(k)\,\frac{(1+f\mu^2/b)^2}{1+(kH_0\sigma_v\mu)^2}. \quad (46)$$

4.2 Fits to the two-dimensional power spectra in redshift slices

We fitted these models to the nine independent two-dimensional power spectra split into tangential and radial components, in order to determine the redshift-space distortion parameters and test the ΛCDM self-consistency relation $\beta \approx \Omega_{\rm m}(z)^{0.55}/b$ as a function of redshift. In this initial analysis, we fixed the matter density parameter $\Omega_{\rm m} = 0.3$ and baryon fraction $\Omega_{\rm b}/\Omega_{\rm m} = 0.166$ [similar to the parameters listed in Komatsu et al. (2009) that provide the best fit to the 5-yr data set of the *Wilkinson Microwave Anisotropy Probe* (*WMAP*); we fix $\Omega_{\rm m} = 0.3$ to match the value assumed for the distance–redshift relation in our power spectrum analysis]. We then varied the redshift-space parameters f and σ_v and the bias factor b, convolving each model power spectrum with the survey selection function for each region and minimizing the χ^2 statistic calculated using the full covariance matrices. For each redshift slice, we combined the results from the three survey regions. The best-fitting models produce a good fit to the measured power spectrum, as evidenced by the values of the χ^2 statistic in the three redshift slices: $\chi^2 = (1113.9, 1229.6, 1069.2)$ for 1137 degrees of freedom.

The measurements of the growth rates at each effective redshift $z_{\rm eff} = (0.42, 0.59, 0.78)$ are $f = (0.73 \pm 0.09, 0.75 \pm 0.09, 0.71 \pm 0.14)$, marginalizing over the parameters σ_v and b, where 1σ error ranges are indicated. These should be compared to the ΛCDM prediction for $\Omega_{\rm m}(0) = 0.3$: $f = (0.72, 0.78, 0.83)$. We find that the model successfully passes this test of self-consistency. Our measurements of the growth rate are compared with the model in Fig. 18 by plotting the quantity $f \times \sigma_{8,{\rm mass}}(z)$ versus redshift. Previously published results are also indicated, as summarized by Song & Percival (2009). The WiggleZ survey data provide a growth measurement across the redshift range $0.4 < z < 0.8$ with a precision similar to previous work at $z < 0.4$. We highlight in particular

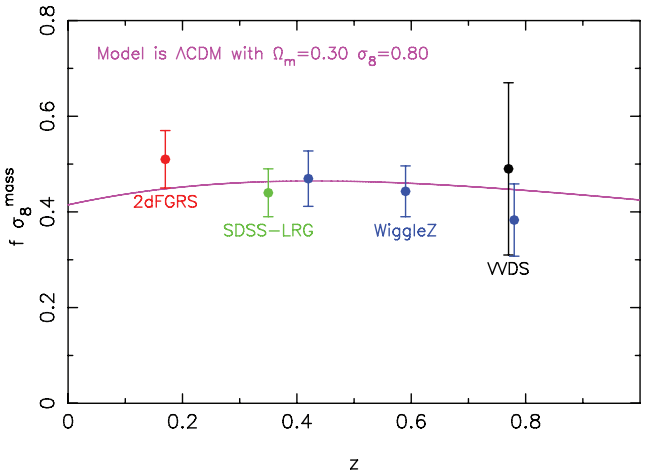

Figure 18. Measurements of the growth rate of structure, f, obtained in three redshift slices by fitting WiggleZ survey data in three survey regions. The values of f are weighted by $\sigma_{8,{\rm mass}}(z)$ as discussed by Song & Percival (2009). The measurements are compared to results previously published for the 2dFGRS, SDSS LRG and VIRMOS-VLT Deep Survey (VVDS) samples, as collected by Song & Percival. A prediction for the ΛCDM cosmological model with $\Omega_{\rm m} = 0.3$ and $\sigma_8 = 0.8$ is overplotted.

the 20 per cent accuracy of our measurement at $z = 0.78$. A future study will perform a more detailed analysis of these results.

The fitted values of the pairwise velocity dispersion in each redshift slice are $\sigma_v = (354 \pm 41, 294 \pm 31, 216 \pm 58)\,h$ km s^{-1} (marginalizing over f and b). We find evidence that the pairwise small-scale velocity dispersion of WiggleZ galaxies systematically decreases with increasing redshift. The measured bias factors for each redshift slice are $b = (0.93 \pm 0.03, 1.08 \pm 0.03, 1.20 \pm 0.06)$ (marginalizing over f and σ_v). We can compare these galaxy bias measurements to those deduced from the WiggleZ survey small-scale correlation function measurements: for three redshift slices similar to those analysed here, Blake et al. (2009) obtained $b = (1.01, 1.27, 1.27)$ (although assuming a higher value of $\sigma_8 = 0.9$). The main cause of this difference is the superior determination of β in the current analysis. Other issues with this comparison include the following: (i) galaxy bias is a scale-dependent function, (ii) small-scale pairwise velocities were not modelled in the Blake et al. (2009) analysis and (iii) the power-law correlation function model assumed in Blake et al. (2009) breaks down at large scales.

4.3 Stacked one-dimensional power spectra

Using these model fits, we can combine the nine one-dimensional power spectrum measurements in the different regions and redshift slices into a single 'stacked' survey one-dimensional power spectrum using inverse-variance weighting. The difficulty with this step is that the power spectrum amplitude in each region is modulated by a different level of convolution with the selection function, as illustrated by Fig. 15. In addition, the shape of the power spectrum varies with redshift in accordance with the differing redshift-space distortion parameters and galaxy bias factors.

Therefore, before combining the results in the different regions and redshift slices, we performed an approximate 'de-convolution' of amplitude by multiplying the power spectra by a correction factor equal to the scale-dependent ratio of the convolved and unconvolved model power spectra, i.e. the ratio of the solid to dashed curves plotted in Fig. 15. [In detail we did not use the model power spectra to generate these corrections but a 'reference' power spectrum in which the baryon oscillation features have been smoothed out, i.e. the 'no-wiggles' power spectrum of Eisenstein & Hu (1998). We preferred to correct the amplitude using a wiggle-free power spectrum to avoid spuriously introducing apparent baryon oscillations into the combined power spectrum]. We additionally corrected the measurement in each Fourier bin by the angle-averaged ratio of the redshift-space galaxy power spectrum (using the best-fitting values of β and σ_v for each redshift slice) to the real-space matter power spectrum at redshift $z = 0.6$. Following these corrections, the nine power spectra 'line up' with consistent shape and amplitude and can be combined. In Fig. 19, we show separate combinations of power spectra across survey regions in each redshift slice and across redshift slices in each survey region. The combination of all nine power spectra is presented in Fig. 20; the lower panel indicates the fractional accuracy of the measurement, which approaches 5 per cent in Fourier bins of width $\Delta k = 0.01\,h$ Mpc^{-1}. The scale dependence of the fractional accuracy is determined by a balance between the increasing number of Fourier modes contributing to each successive bin (tending to decrease the error) and the increasing importance with k of shot noise relative to cosmic variance (tending to increase the error). Finally, in Fig. 21 we display the two-dimensional power spectra for each redshift slice, combining different regions in the manner described above.

4.4 Fits for matter and baryon densities

As a final exercise, we fitted the measured power spectra for the cosmological matter and baryon densities (parametrized by Ω_m and $f_b = \Omega_b/\Omega_m$). We tried three different initial approaches to this analysis, with increasing degrees of sophistication.

(i) First, we generated unconvolved, real-space, non-linear power spectra and fitted the combined survey data points plotted in the upper panel of Fig. 20 by varying Ω_m, f_b and the bias factor b.

(ii) Secondly, we fitted the convolved, redshift-space one-dimensional power spectra in each of the survey regions and redshift slices, fixing the redshift-space distortion parameters β and σ_v at the best-fitting measurements using the two-dimensional power spectrum fits at each redshift and varying Ω_m, f_b and b.

(iii) Thirdly, we fitted the convolved, redshift-space two-dimensional power spectra, fixing the value of σ_v at the best-fitting values. We varied Ω_m, f_b and the bias factor b, determining the value

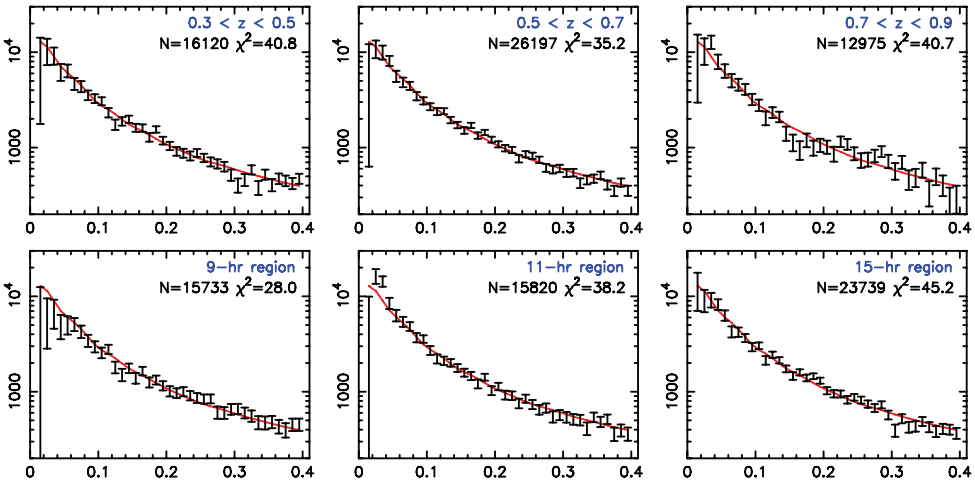

Figure 19. The power spectra determined by combining the measurements in the different survey regions (for each redshift slice) and different redshift slices (for each survey region). Before combination, we adjust the shapes of the power spectra to allow for the differing degrees of convolution with the selection function and the differing redshift-space effects. The solid line in the panel has been generated by combining the best-fitting model power spectra in a similar manner. The x-axis and y-axis of each panel are Fourier wavescale k in units of h Mpc^{-1} and power spectrum amplitude $P(k)$ in units of h^{-3} Mpc^3, respectively.

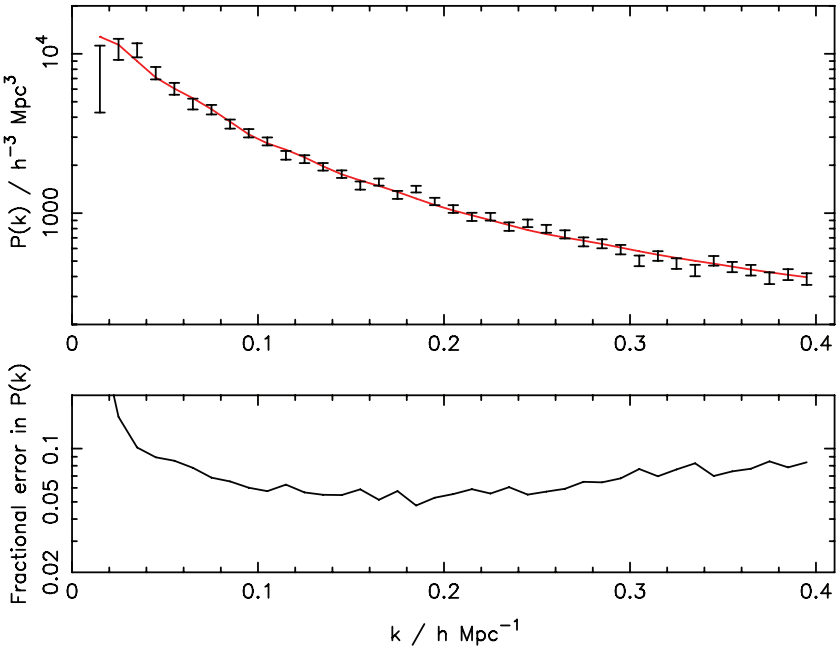

Figure 20. Upper panel: the power spectrum determined by combining the measurements in the different survey regions and redshift slices analysed in this paper using inverse-variance weighting. Before combination, we adjust the shapes of the power spectra to allow for the differing degrees of convolution with the selection function and the differing redshift-space effects. The solid line in the panel has been generated by combining the best-fitting model power spectra in a similar manner. Lower panel: the fractional error in the combined power spectrum as a function of Fourier wavenumber k.

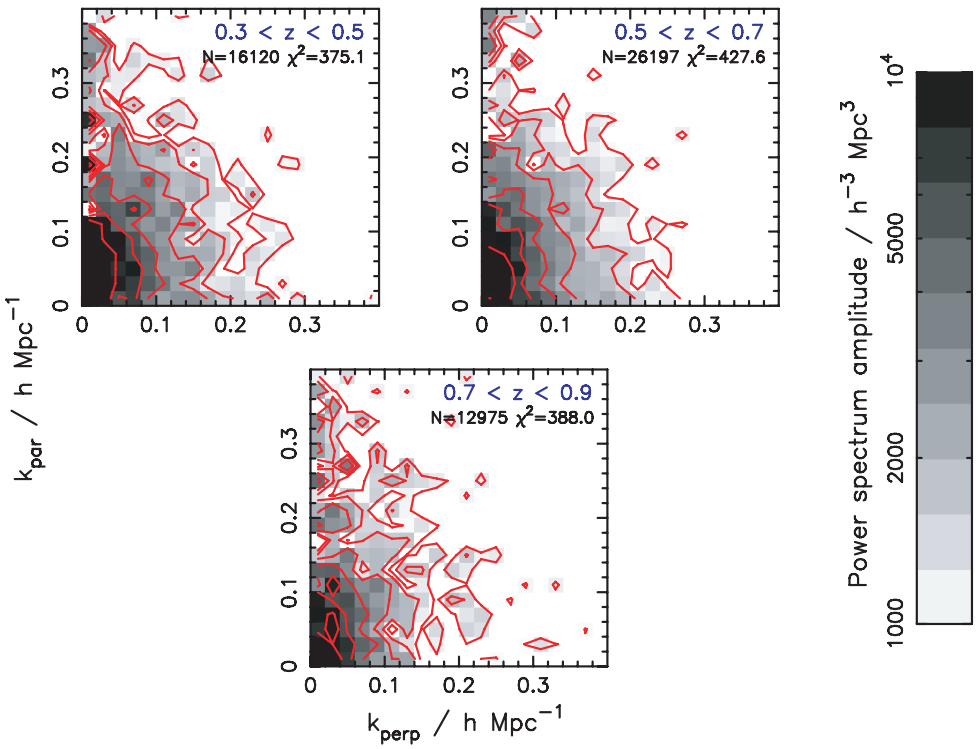

Figure 21. The two-dimensional galaxy power spectra for each of the redshift slices analysed in this paper, obtained by combining measurements in different survey regions, and plotted as a function of wavevectors ($k_{\rm perp}$, $k_{\rm par}$) tangential and radial to the line of sight, respectively. The function is represented using both grey-scale and contours; the contour levels are logarithmically spaced between $P = 1000$ and $10\,000\,h^{-3}$ Mpc^3. The non-circularity of the contours encodes the imprint of large-scale galaxy peculiar velocities, as discussed in the text.

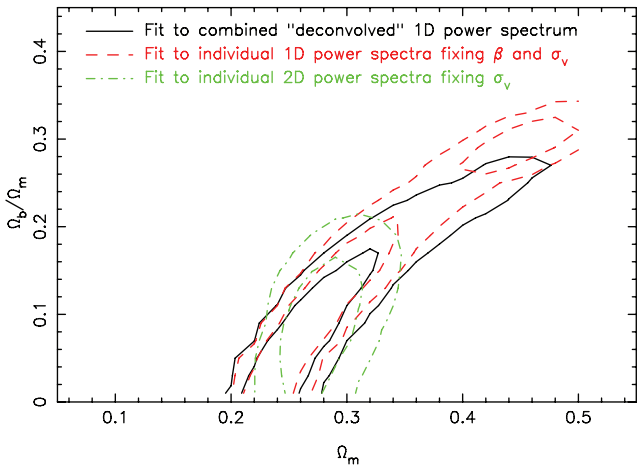

Figure 22. Probability contours of Ω_m and Ω_b/Ω_m fitting to WiggleZ survey power spectra using the three different approaches described in the text. The inner and outer contours for each set enclose 68 and 95 per cent of the likelihood, respectively.

$\beta = \Omega_m(z)^{0.55}/b$ in each case (assuming the ΛCDM model). For each different value of Ω_m, we scaled σ_8 assuming the '*WMAP* normalization' (section 5.5 of Komatsu et al. 2009) and also scaled the geometry of the survey box in accordance with each trial cosmology: given a fiducial co-moving distance D_{fid} and Hubble parameter H_{fid} for a redshift slice calculated using $\Omega_m = 0.3$, and also given trial values D, H corresponding to a different value of Ω_m, the width of Fourier bins tangential and radial to the line of sight scales as D/D_{fid} and H_{fid}/H, respectively; furthermore, the volume of the box (hence amplitude of the measured power spectrum) scales as $(D/D_{fid})^2 \times (H_{fid}/H)$.

Fig. 22 displays the probability contours in the two-dimensional space of Ω_m and $f_b = \Omega_b/\Omega_m$, marginalizing over the bias factor, for each of the three approaches described above. The different methods produce broadly consistent results, and the best-fitting values are in good agreement with those determined from the latest measurements of the temperature fluctuations of the cosmic microwave background radiation (Komatsu et al. 2009).

The probability contours in Fig. 22 display evidence of the well-known degeneracy between Ω_m and Ω_b/Ω_m in the determination of the overall shape of the matter power spectrum, which is exacerbated by the fact that we cannot yet detect the imprint of the baryon acoustic oscillations in our power spectrum measurement. This degeneracy will be broken as the WiggleZ survey progresses.

5 CONCLUSIONS

In this paper, we have described our method of determining the selection function of the WiggleZ Dark Energy Survey and have presented the current measurement of the large-scale galaxy power spectrum using 56 159 redshifts of bright emission-line galaxies spanning redshifts $0.3 < z < 0.9$. This sample constitutes approximately 25 per cent of the final WiggleZ survey. We have quantified and categorized the redshift blunder rate and determined its effect on the power spectrum measurement via analytical calculations and detailed simulations. We conclude the following.

(i) The selection function of the WiggleZ survey is complicated by the proximity of the faint magnitude threshold to the completeness limit of the input catalogues, in particular for the *GALEX* UV data. We quantified the incompleteness in the parent target catalogue as a function of *GALEX* exposure time and Galactic extinction via fitting formulae.

(ii) We adopted a Monte Carlo technique to determine the relative completeness of the spectroscopic follow-up at any position. This technique allows for the complex overlapping of survey pointings and for the systematic variation of redshift completeness across the 2° field of view of the instrument. We also allowed for the magnitude prioritization of the spectroscopic follow-up which results in a position-dependent galaxy redshift distribution.

(iii) The WiggleZ survey contains redshift blunders resulting from emission-line confusion (most significantly, [O III], Hβ and Hα mis-identified as [O II]) and from sky emission lines mis-identified as [O II]. The overall blunder rate is about 5 per cent. The effect of the redshift blunders on the power spectrum measurement is well approximated as a constant reduction in amplitude for scales $k > 0.05\,h$ Mpc^{-1} combined with an enhanced level of reduction for large scales $k < 0.05\,h$ Mpc^{-1}.

(iv) We measured one-dimensional (angle-averaged) and two-dimensional (binned in tangential and radial modes) galaxy power spectra for nine independent survey regions and redshift slices using the method of FKP. The one-dimensional power spectrum for the whole sample, combining these measurements, has a fractional accuracy of about 5 per cent in Fourier bins of width $\Delta k = 0.01\,h$ Mpc^{-1}. The two-dimensional power spectra show the expected anisotropic signatures of redshift-space distortions due to large-scale coherent infall and small-scale virialized motions.

(v) The power spectrum data are well described by a model power spectrum with matter and baryon densities consistent with those determined from observations of the cosmic microwave background radiation. The model includes non-linear corrections, redshift-space distortions and a linear galaxy bias factor.

(vi) The two-dimensional power spectra allow us to measure the growth rate of structure across the redshift range $0.4 < z < 0.8$. We obtain results similar in precision to previous determinations at $z < 0.4$, including a measurement at $z = 0.78$ with 20 per cent accuracy.

Future studies will present full cosmological parameter fits and combinations of these results with other data sets, including implications for the growth of cosmic structure and Gaussianity of the initial conditions, and extend these analyses to the final WiggleZ survey catalogues.

ACKNOWLEDGMENTS

We thank an anonymous referee for useful comments on the submitted version of this paper.

We acknowledge financial support from the Australian Research Council through Discovery Project grants funding the positions of SB, MP, GBP and TD. SC acknowledges the support of the Australian Research Council through a QEII Fellowship. MJD thanks the Gregg Thompson Dark Energy Travel Fund for financial support.

GALEX is a NASA Small Explorer, launched in 2003 April. We gratefully acknowledge NASA's support for construction, operation and science analysis for the *GALEX* mission, developed in cooperation with the Centre National d'Etudes Spatiales of France and the Korean Ministry of Science and Technology.

Finally, the WiggleZ survey would not be possible without the dedicated work of the staff of the Anglo-Australian Observatory in the development and support of the AAOmega spectrograph, and the running of the AAT.

REFERENCES

Bardeen J. M., Bond J. R., Kaiser N., Szalay A. S., 1986, ApJ, 304, 15
Blake C. A., Bridle S. L., 2005, MNRAS, 363, 1329
Blake C. A., Glazebrook K., 2003, ApJ, 594, 665
Blake C. A., Collister A., Bridle S., Lahav O., 2007, MNRAS, 374, 1527
Blake C. A., Collister A., Lahav O., 2008, MNRAS, 385, 1257
Blake C. A. et al., 2009, MNRAS, 395, 240
Bond J. R., Efstathiou G., 1984, ApJ, 285, 45
Cole S. et al., 2005, MNRAS, 362, 505
Colless M. et al., 2001, MNRAS, 328, 1039
Conway E. et al., 2005, MNRAS, 356, 456
Cresswell J. G., Percival W. J., 2009, MNRAS, 392, 682
Croft R., Weinberg D. H., Bolte M., Burles S., Hernquist L., Katz N., Kirkman D., Tytler D., 2002, ApJ, 581, 20
Dekel A., Lahav O., 1999, ApJ, 520, 24
Drinkwater M. et al., 2010, MNRAS, 401, 1429
Eisenstein D. J., Hu W., 1998, ApJ, 518, 2
Eisenstein D. J. et al., 2001, AJ, 122, 2267
Eisenstein D. J. et al., 2005, ApJ, 633, 560
Elgaroy O. et al., 2002, Phys. Rev. Lett., 89, 1301
Feldman H. A., Kaiser N., Peacock J. A., 1994, ApJ, 426, 23 (FKP)
Fry J. N., Scherrer R. J., 1994, ApJ, 429, 36
Glazebrook K., Blake C. A., 2005, ApJ, 631, 1
Gott J. R., Dickinson M., Melott A. L., 1986, ApJ, 306, 341
Guzzo L. et al., 2008, Nat, 451, 541
Hamilton A. J. S., 1992, ApJ, 385, 5
Hamilton A. J. S., 2001, MNRAS, 322, 419
Hawkins E. et al., 2003, MNRAS, 346, 78
Heath D. J., 1977, MNRAS, 179, 351
Holtzman J. A., 1989, ApJS, 71, 1
Hoyle F., Outram P. J., Shanks T., Croom S. M., Boyle B. J., Loaring N. S., Miller L., Smith R. J., 2002, MNRAS, 329, 336
Hu W., Haiman Z., 2003, Phys. Rev. D, 68, 063004
Hu W., Sugiyama N., 1996, ApJ, 471, 542
Huetsi G., 2006, A&A, 459, 375
James J. B., Lewis G. F., Colless M., 2007, MNRAS, 375, 128
Jing Y., 2005, ApJ, 620, 559
Jeong D., Komatsu E., 2006, ApJ, 651, 619
Komatsu E. et al., 2009, ApJS, 180, 330
Lewis A., Challinor A., Lasenby A., 2000, ApJ, 538, 473
Linder E. V., Jenkins A., 2003, MNRAS, 346, 573
McDonald P., 2007, Phys. Rev. D, 75, 3514
McDonald P. et al., 2005, ApJ, 635, 761
McDonald P. et al., 2006, ApJS, 163, 80
Morrissey P. et al., 2007, ApJS, 173, 682
Nishimichi T., Kayo I., Hikage C., Yahata K., Taruya A., Jing Y. P., Sheth R. K., Suto Y., 2007, PASJ, 59, 93
Outram P. J., Hoyle F., Shanks T., Croom S. M., Boyle B. J., Miller L., Smith R. J., Myers A. D., 2003, MNRAS, 342, 483
Padmanabhan N. et al., 2007, MNRAS, 378, 852
Peacock J. A., Dodds S. J., 1994, MNRAS, 267, 1020
Percival W., 2005, A&A, 443, 819
Percival W., White M., 2009, MNRAS, 393, 297
Percival W. et al., 2001, MNRAS, 327, 1313
Percival W. et al., 2002, MNRAS, 337, 1068
Percival W. et al., 2007a, ApJ, 657, 645
Percival W. et al., 2007b, MNRAS, 381, 1053
Pope A. et al., 2004, ApJ, 607, 655
Ross N. et al., 2009, ApJ, 697, 1634
Sanchez A., Cole S., 2008, MNRAS, 385, 830
Scherrer R. J., Weinberg D. H., 1998, ApJ, 504, 607
Sefusatti E., Komatsu E., 2007, Phys. Rev. D, 76, 3004
Seljak U., Zaldarriaga M., 1996, ApJ, 469, 437
Seljak U. et al., 2005, Phys. Rev. D, 71, 3515
Seo H.-J., Eisenstein D. J., 2003, ApJ, 598, 720
Smith R. E. et al., 2003, MNRAS, 341, 1311
Smith R. E., Scoccimarro R., Sheth R. K., 2007, Phys. Rev. D, 75, 3512
Song Y.-S., Percival W. J., 2009, J. Cosmology Astropart. Phys., 10, 4
Tadros H., Efstathiou G., 1996, MNRAS, 282, 1381
Tegmark M., 1997, Phys. Rev. Lett., 79, 3806
Tegmark M., Bromley B. C., 1999, ApJ, 518, 69
Tegmark M. et al., 2004a, ApJ, 606, 702
Tegmark M. et al., 2004b, Phys. Rev. D, 69, 3501
Tegmark M. et al., 2006, Phys. Rev. D, 74, 3507
Verde L. et al., 2002, MNRAS, 335, 432
Wang Y., 2008, J. Cosmology Astropart. Phys., 05, 021
White M., Song Y.-S., Percival W. J., 2009, MNRAS, 397, 1348
Wild V. et al., 2005, MNRAS, 356, 247
Xu K. et al., 2005, ApJ, 619, 11
York D. G. et al., 2000, AJ, 120, 1579
Zehavi I. et al., 2005, ApJ, 630, 1

This paper has been typeset from a TEX/LATEX file prepared by the author.